

EÖTVÖS LORÁND UNIVERSITY
FACULTY OF SCIENCE
MASTER'S THESIS

Angular-Correlation Measurements in Ultra-relativistic Heavy-ion Collisions

Balázs Endre Szigeti
Physics MSc. II.



Supervisor:

Mónika Varga-Kőfaragó, PhD.
Wigner Research Centre for Physics
Research fellow

Consulent:

Márton Imre Nagy, PhD.
Eötvös Loránd University
Associate professor

Abstract

One of the main goals of research on heavy-ion physics is to study the properties of the quark-gluon plasma, ultra-relativistic heavy-ion collisions are widely used for this purpose. The ALICE detector at the CERN Large Hadron Collider is dedicated to investigate these collision. Jets are produced in the early stage of the collisions and they interact with the hot and dense QCD medium formed in relativistic heavy-ion collisions. For several years great effort has been devoted to study jets, which provide important information about the quark-gluon plasma. In this thesis, I present after a short introduction to the experimental and Monte Carlo simulation techniques used for the analysis of ultra-relativistic collision. My analysis on the interaction of jets with the medium I study two-particle angular correlations in Pb-Pb collisions at $\sqrt{s_{NN}} = 5.02$ TeV energy at the ALICE experiment. The aim of this work is to analyse the transverse momentum (p_T) and particle species dependence of the medium interaction as a function of the azimuthal angle ($\Delta\varphi$) and pseudorapidity ($\Delta\eta$) differences in two-particle angular correlations. In these measurements, jets manifest themselves as a peak around $\Delta\varphi = 0$, $\Delta\eta = 0$. Quantitative information can be obtained quark-gluon plasma by fitting this jet peak, which is one of the signature of the quark-gluon plasma. These results showed that the jet peak are broadens and becomes asymmetric in central collision at low transverse momentum. Identified angular-correlation results indicate that the width and shape of the near-side jet peak have a clear particle species dependence.

Contents

1	Introduction	3
2	Theoretical background	4
2.1	Centrality	5
2.2	Jets in high-energy collision	5
2.3	Azimuthal flow in high-energy collision	8
3	Monte Carlo simulations for high-energy collisions	10
3.1	A Multi-Phase Transport model (AMPT)	12
4	The ALICE experiment at the CERN LHC	13
4.1	Tracking detectors	14
4.2	Particle identification	15
4.3	Electromagnetic Calorimeter	15
4.4	Centrality measurements	16
5	Analysis method	16
5.1	Two-particle angular correlations	18
5.2	Vertex and track reconstruction	23
5.3	Particle identification	24
5.4	Systematic uncertainties	24
5.5	Tracking inefficiencies	44
6	ALICE data analysis	45
7	Results of the AMPT simulations	50
8	Summary	60
9	Összefoglalás	61

1 Introduction

"An experiment is a question which science poses to Nature, and a measurement is the recording of Nature's answer."

— Max Planck, 1949

The nuclear and particle physics experiments from the past century proved that protons and neutrons are not elementary particles, instead they are built up by quarks and gluons, together referred to as partons [1]. The interactions between them governed by the strong force and its relativistic quantum field theory description is called quantum-chromodynamics (QCD). The experimental results showed that at low energy free quarks cannot be observed. Since quantum-chromodynamics can be renormalised it indicates that the coupling strength between the partons depends on the interaction scale, which is called running coupling. At sufficiently large energy we can observe that the coupling becomes small enough that the interaction will be negligible, which is called asymptotic freedom [2]. Astrophysical researches showed that the pressure was many orders of magnitude (10^{27}) higher than the current level. At that time the matter of the Universe existed in a strongly coupled asymptotically free state that is commonly referred to as the quark-gluon plasma. Then the Universe expanded and cooled radically, therefore the coupling between the quarks grows and the coloured particles converted into colourless states. This process is called hadronisation [2].

Dedicated experiments are built at large particle accelerators all around the world. These experiments play an important role in the investigation of the quark-gluon plasma. These dedicated experiments are for instance the ALICE experiment at the Large Hadron Collider (LHC) at the European Organisation for Nuclear Research (CERN) or the PHENIX (Pioneering high-energy Nuclear Interactions eXperiment) and the STAR (Solenoidal Tracker at RHIC) experiment at the Relativistic heavy-ion collider at the Brookhaven National Laboratory. The main goal of these experiments is to reproduce the conditions of matter after the Big Bang and to explore the phase diagram of strongly interacting matter, which can be seen in Fig. 1. [3]. Throughout this thesis I will to give a short introduction to the widely used experimental and Monte Carlo methods in heavy-ion physics and a detailed description of unidentified and identified two-particle angular correlations. Finally, in Sec 6 I will present my analysis results.

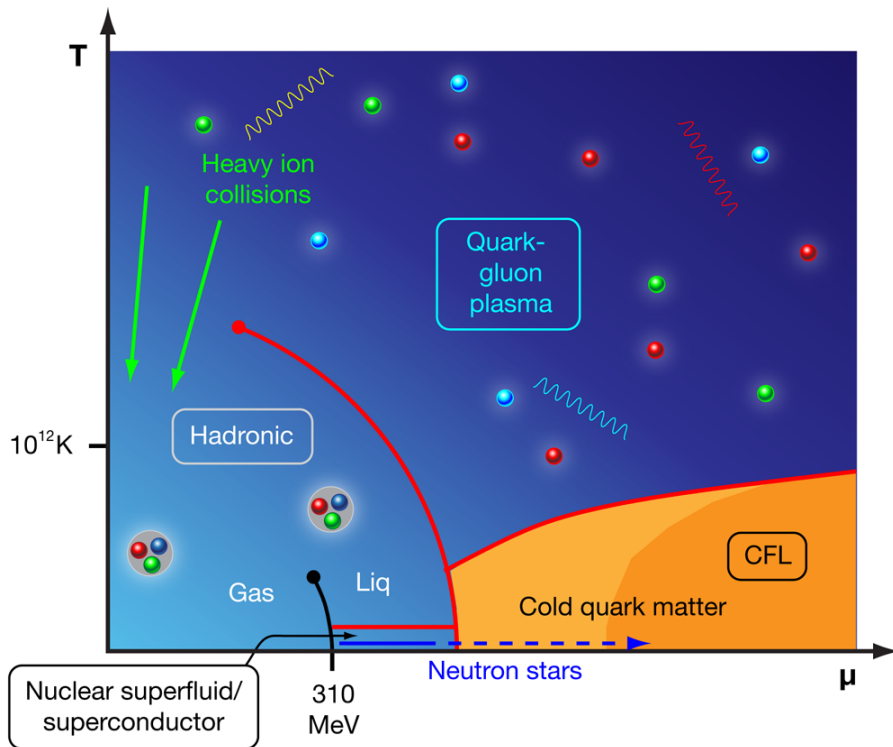


Figure 1: The phase diagram of strongly interacting matter [4].

2 Theoretical background

Research of heavy-ion physics is focused on the investigation of hadronic matter and the strong interaction under extreme conditions. As it was previously mentioned heavy-ion collisions provide a good opportunity to study the interaction between partons at low distance scales. Previous research demonstrated that the quark-hadron phase transition takes place at $1 \text{ GeV}/\text{fm}^3 \leq \epsilon \leq 3 \text{ GeV}/\text{fm}^3$ energy density, in other words when the coupling constant reaches the $\alpha_s \approx 0.12$ value. This value corresponds to $150 \text{ MeV} \leq T_c \leq 200 \text{ MeV}$ critical temperature [5]. This particular state of matter is commonly referred to as the quark-gluon plasma (Fig. 1). If the coupling constant is sufficiently small, the particular system can be treated perturbatively. Theoretical considerations suggested that in these cases a weakly coupled gas-like state will be formed. However, it has been found by experiments that the formed matter is strongly

coupled and has superfluid properties, and therefore it has been referred to as sQGP later [6]. It is important to notice that we can only detect colourless final states in experimental measurements as a consequence of quark confinement, which causes significant difficulties. For this reason, it is problematic to gain information about the coloured partons from the hadronic final states. Moreover, in the hadronic phase and during the hadronisation the system is not perturbative, therefore the theoretical description of these systems is more complicated and required phenomenological (Monte Carlo simulations) approach.

2.1 Centrality

An important property of heavy-ion collisions is the extent the colliding nuclei overlap, which determines the space where QGP is formed. This can be characterised by the collision parameter b , which measures the distance between the centres of the colliding nuclei. Even though it is a well defined geometrical quantity, it cannot be measured directly, thus we have to introduce the concept centrality that can be expressed in terms of [7],

$$c = \frac{1}{\sigma_{AA}} \int_0^b \frac{d\sigma}{db'} db', \quad (1)$$

where $d\sigma$ is the differential cross section and the σ_{AA} is the geometrical cross section of the nucleon-nucleon collision. In general, centrality can not be determined based on this definition. Due to this reason, we have to express centrality with quantities that depend on the collision parameter monotonically. These quantities are for instance, the multiplicity (N_{ch}), or in other words the number of generated charged particles or the energy released in the Zero-Degree Calorimeter, detailed in section 4.

$$c \approx \frac{1}{\sigma_{AA}} \int_0^{E_{ZDC}^{THR}} \frac{d\sigma}{dE_{ZDC}} dE_{ZDC} \approx \frac{1}{\sigma_{AA}} \int_0^{N_{ch}^{THR}} \frac{d\sigma}{dN_{ch}} dN_{ch} \quad (2)$$

Furthermore, we can say that the collision is central if the collision parameter is small and the collision is peripheral if the b is large.

2.2 Jets in high-energy collision

QCD hard processes can occur at high-energy in hadron-hadron, lepton-lepton and lepton-hadron collisions. A process is referred to as a hard scattering if the 4-momentum squared transfer (Q^2) is comparable with the QCD scale Λ^2 . In this regime, the system can be described

with perturbative methods. Partons with high transverse momenta (p_T) are created in hard processes. These high p_T quark or gluon pairs are flying "back-to-back" according to the 4-momentum conservation law. During the propagation of these colour charged particles a narrow flux-tube (usually referred to as string) is generated. As a result, if the energy density of the generated colour field is sufficiently large, a quark-antiquark pair will be created. During the propagation, gluons are emitted by the outgoing quarks. Also these gluons can produce quark-antiquark pairs and these pairs are spatially correlated to the original gluon [8]. This process will continue until the moment when the average transverse momentum of these particles is sufficiently small and the partons recombine into colourless hadrons. The final hadrons are detected inside a well-defined cone - commonly referred as the jet-cone -, and this spray of particles is called jets. In hadronic scatterings the jet production cross section is known and it is given by

$$\sigma_{ij \rightarrow k} = \sum_{i,j} \int dx_1 dx_2 d\hat{t} f_i^1(x_1, Q^2) f_j^2(x_2, Q^2) \frac{d\hat{\sigma}_{ij \rightarrow k}}{d\hat{t}}. \quad (3)$$

In this expression x is the longitudinal momentum fraction [9], Q^2 is the momentum transfer, $d\hat{\sigma}_{ij \rightarrow k}$ is the perturbative elementary cross section for the given reaction and finally $f_i^a(x, Q^2)$ is the parton distribution function for finding particle species i in a beam, a [10].

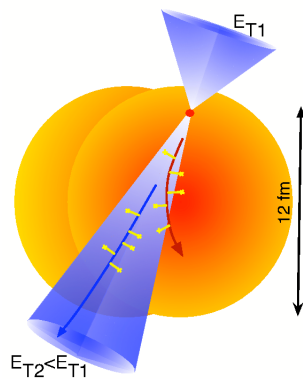


Figure 2: Schematic illustration of the model of jet energy-loss [11].

The transverse momentum distribution measurements of back-to-back jets showed high asymmetry between the detected momentum in heavy-ion collisions, in contrast to proton-proton collisions, where the energy of the two jets are roughly the same. This phenomenon

lead us to presume that in the heavy-ion collision the QGP has been formed, the interaction of jets with the hot QCD medium and the momentum exchange lead to a parton-energy loss, which altered the distributions of fragmentation products in the final state [8]. This effect is usually referred to as jet-quenching [12], and has been depicted on Fig. 2. As can be seen in Fig. 1, the value of the energy loss of the jet at the bottom is smaller, because it has propagated longer in the QGP than the upper one[13].

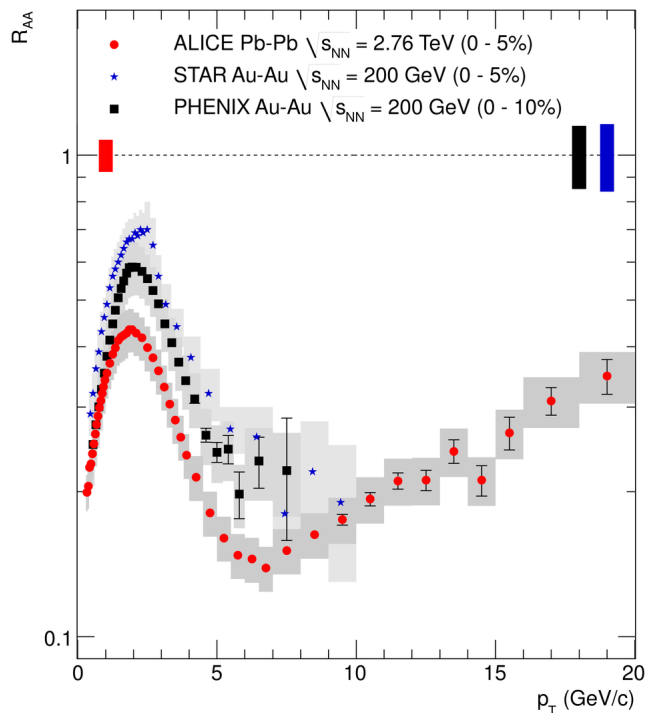


Figure 3: The measured nuclear modification factor (R_{AA}) values are measured in central nuclei collision at different experiments [14].

The nuclear modification factor (R_{AA}) was introduced to quantitatively describe the jet energy loss. This quantity gives the ratio between the detected yields in heavy-ion collisions and in proton-proton collisions, normalised by the average number of binary nucleon-nucleon collisions ($\langle N_{\text{binary}} \rangle$) in a given centrality class. Based on this the equation can be expressed in terms of:

$$R_{AA}(p_T) = \frac{1}{\langle N_{\text{binary}} \rangle} \frac{(1/N_{\text{event}}^{\text{AA}}) d^2 N_{\text{charged}}^{\text{AA}} / d\eta dp_T}{(1/N_{\text{event}}^{\text{PP}}) d^2 N_{\text{charged}}^{\text{PP}} / d\eta dp_T}, \quad (4)$$

where p_T is the transverse momentum with the following definition $p_T = \sqrt{p_x^2 + p_y^2}$, where the z -axis is parallel to the beam and N_{events} is the number of events. Furthermore, we can define the azimuth angle and the pseudorapidity in the following way:

$$\varphi = \arctan \left[\frac{p_y}{p_x} \right] \quad \eta = -\ln \left[\tan \left(\frac{\theta}{2} \right) \right]. \quad (5)$$

The formula of Eq. 4 captures that if the nuclear modification factor is equal to one, then heavy-ion collision can be treated as a superposition of proton-proton collisions. Experimental results show that this requirement is not fulfilled as the measured values of R_{AA} differ significantly from one. Fig. 3. compares the values of the nuclear modification factor in different experiments (ALICE, STAR, PHENIX) and with different nuclei (RHIC: AuAu, LHC: PbPb) at different colliding energy per nucleon pair (LHC: $\sqrt{s_{NN}} = 2.76$ TeV, RHIC: $\sqrt{s_{NN}} = 200$ GeV). Fig. 3. illustrates well that the R_{AA} as a function of p_T follows similar trends regardless of the colliding energy and the beam type and it has a clear minimum at approximately $p_T \approx 6$ GeV/ c .

2.3 Azimuthal flow in high-energy collision

In non-central heavy-ion collisions the created quark gluon plasma has an ellipsoidal spatial symmetry. This effect is illustrated in Fig. 4. If the formed quark gluon plasma is strongly coupled, this initial spatial asymmetry will appear in momentum space. In addition to this, extra higher-order symmetries be also observed. These effects are commonly referred to as *asimuthal flow*. If we would like to quantify this phenomenon, we have to expand the transverse momentum distribution of the final hadrons into a Fourier-series by the azimuth-angle (φ) [15].

$$N(p_T, \varphi) = N(p_T) \sum_{n=1}^{\infty} (1 + v_n \cos(n\varphi)) \quad (6)$$

The first significant term is the one containing v_2 component, which determines an ellipsoidal deviation from the spherical symmetry in the transverse plane. This is called elliptical flow,

which refers to the elliptical nature of the transverse momentum distribution. The higher order terms in v_n can also be measured. The v_3 term comes from the fluctuations of the initial protons and neutrons in the nuclei and it is called *triangular flow*. The further terms can also be significant and these are related to higher order symmetry properties.

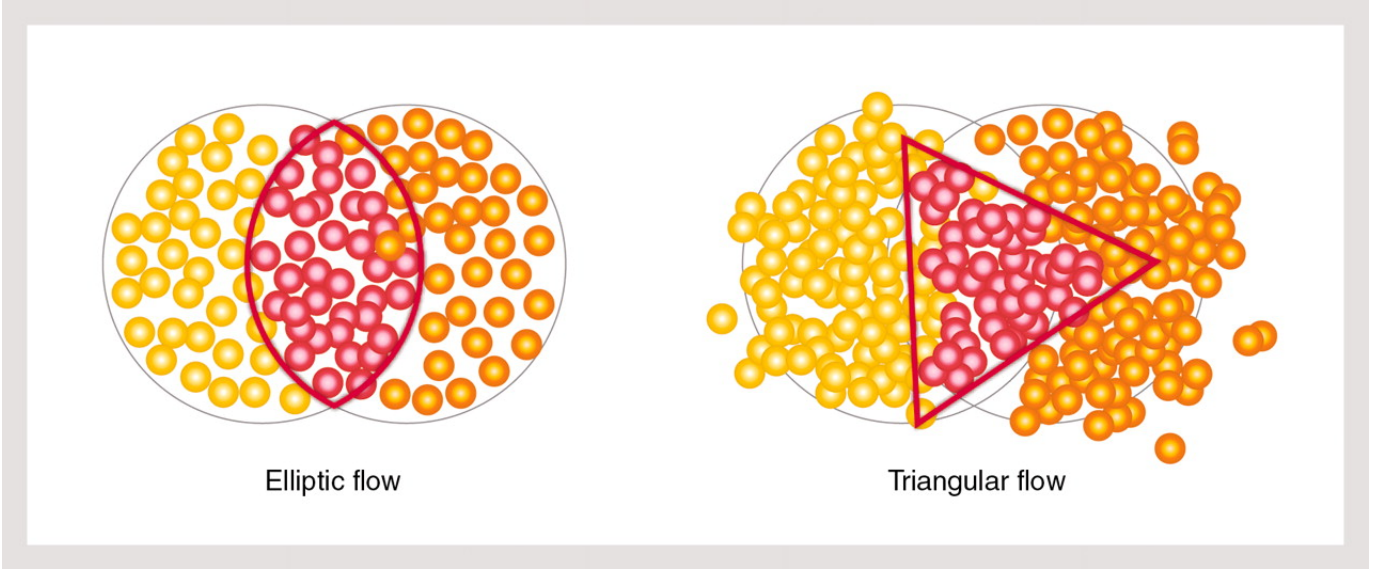


Figure 4: Schematic illustration of the structure of non-central heavy-ion collisions and the symmetries related to v_2 and v_3 terms [15].

The Eq. 6. equation holds only if the transverse distribution changes slowly in pseudo-rapidity ($\Delta\eta$). It is also true, that the v_n coefficients heavily depend on p_T . Fig. 5. shows the fit of the different v_n values of the data measured in Pb-Pb collisions at 2.76 TeV the centre of mass energy in the ALICE experiment the case of single event. The green dashed line indicates the fit of the v_2 parameter, the grey dotted line indicates the v_3 component and finally ρ_{ch} indicates the multiplicity density. The sine terms were not listed in the Eq. (6). since these are equal to zero due to symmetry reasons.

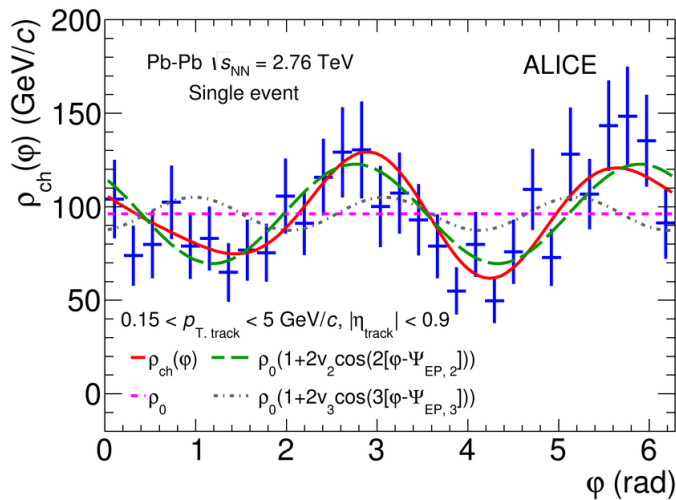


Figure 5: Illustration of the azimuthal flow in one event [16].

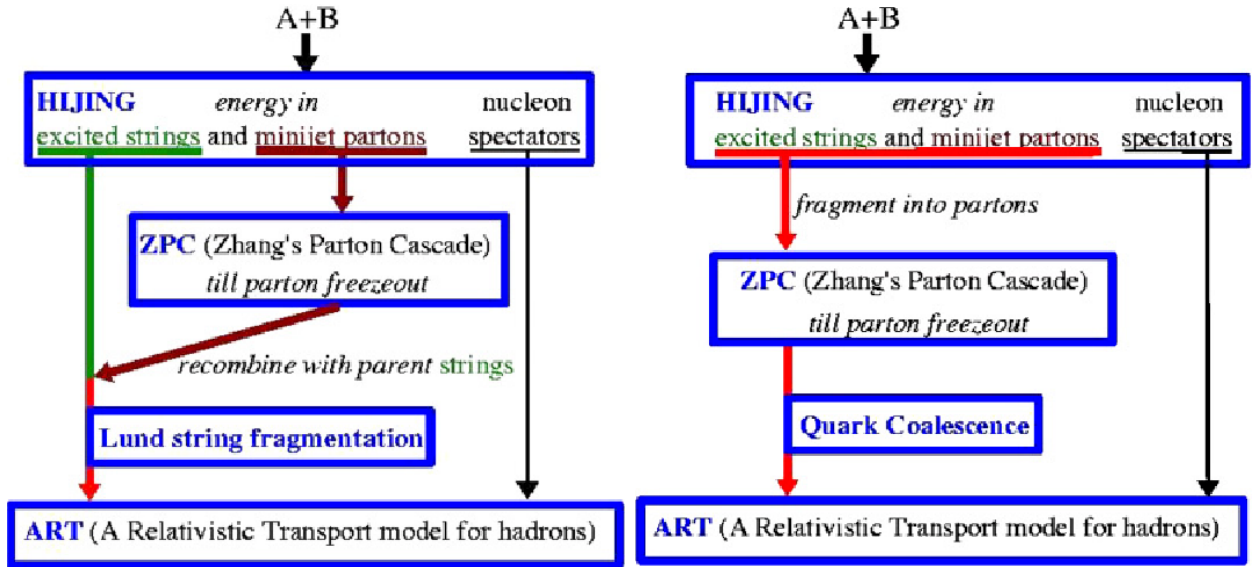
3 Monte Carlo simulations for high-energy collisions

As was mentioned the theoretical description of the final states of high-energy collision is an extremely challenging problem. In an event usually hundreds of new particles are produced and the momentum transfer in the parton interaction ranges over several orders of magnitude. If we would like to calculate the relevant cross sections and invariant matrix elements for all of these interactions, it would not be possible in first-order perturbation. On top of that non-perturbative processes are also involved in QCD interactions. The key method to handle this seemingly unsolvable problem is factorisation. It allows us to separate the processes of interest into different regimes according to the scale of the momentum transfer takes place on. There are three main distinguished regime. Firstly, at the highest scales the partons of the incoming hadronic beams produce a small number of elementary particles with relatively high energies, these processes can be treated perturbatively. Secondly, at the lowest scales of the order of 1 GeV, partons and final hadrons interact with each other non-perturbatively. These interactions can not be evaluated from first principles, so they have to be modelled with phenomenological approaches. Finally, the hard and soft regimes are separated, but they can be linked with each other with evolutionary processes. This kind of picture gives us a very powerful tool to describe ultra-relativistic hadronic collisions and eventually this procedure suits well to Monte Carlo simulation techniques well [17].

If we consider a single proton-proton collision, the initial distribution of partons within the proton have to be determined before the collision. Therefore, Parton Distribution Functions (PDFs) are used to describe the likelihood that the quarks and gluons are found in a given momentum fraction [18]. If we would like to consider nucleon-nucleon collisions we have to determine the initial distribution of protons and neutrons, a widely used of this is the Wood–Saxon potential [19]. The modeling of the initial phase of heavy-ion collisions and the determination of the relevant 'geometric' parameters - such as the impact parameter (b), the number of participating nuclei (N_{part}) and the number of binary nucleon-nucleon collision (N_{coll}) - are commonly based on an optical model, like the Glauber-model [20]. Given these parameters, the initial hard scattering and the parton showers are simulated by the model chosen to describe the hard regime (usually Leading Order calculation). The next step is to describe the transition from the final radiation into the hadrons based on a hadronisation model, like string-model, or cluster-model for example [21]. After the hadronisation there may be unstable hadrons that will decay. This would be the full description of one hadronic collision if only one hard scattering took place. However, the other partons and nuclei can also interact in physical realisation of the hadronic collision. These interactions are commonly referred to as the bulk [22]. These processes provide significant contribution to the background of any measured phenomena, so these have to be simulated as well. In addition to this, it is also possible that in one event more than one initial hard scatterings occur. This property of the collision can be modelled by Multiple Parton Interactions (MPI) [23]. Many studies have been published on these models not being enough to describe the dynamics of the formulated QGP and the interactions between jets and QGP in heavy-ion collisions. In my work, I used two different Monte Carlo event generators to study the effects of flow on identified and unidentified angular-correlations.

3.1 A Multi-Phase Transport model (AMPT)

The AMPT model is dedicated to describe nucleon-nucleon and proton-nucleon collisions from $\sqrt{s_{NN}} = 5$ GeV up to 5.5 TeV centre-of-mass energy, where strings (soft part) and minijet (hard part) production dominate the initial energy density distribution [24]. AMPT simulates the interaction between (mini)jets and the hot and dense QCD medium via four stages: initial conditions, partonic interactions, hadronisation and hadronic scatterings. The initial conditions for the minijets and excited strings are obtained from the HIJING model[24]. In the next step, the partonic interaction modelled by the Boltzmann equation of the quarks and gluons. It is solved by the Zhang's Parton Cascade model (ZPC). After the partonic interactions, the hadronisation can be done by the quark coalescence or the Lund-string fragmentation model depending on the specific settings [21]. Furthermore, hadronic interactions can also be added. This hadronic phase is modelled by the ART (A Relativistic Transport) model. Overall, I used three different setup to simulate Pb-Pb collisions at $\sqrt{s_{NN}} = 5.02$ TeV energy. The corresponding configurations for the first two setups are depicted in Fig. 6 and for the third case I used the string melting on setting without the ART model [24].



(a) String Melting Off

(b) String Melting On

Figure 6: The AMPT string melting off/on configurations [24].

4 The ALICE experiment at the CERN LHC

The ALICE (A Large Ion Collider Experiment) is located in the Large Hadron Collider (LHC). The LHC is the main beam accelerator and storage ring of the facility of the European Organisation for Nuclear Research (CERN) near Geneva, Switzerland [25]. It is a synchrotron with two beams of particles circulating in opposing directions. It is capable to provide proton collision at a maximum centre-of-mass energy of $\sqrt{s} = 14$ TeV and Pb-Pb collision at a the centre-of-mass energy per nucleon pair of $\sqrt{s_{NN}} = 5.02$ TeV, it can also be used to provide asymmetric collisions of protons and heavy-ions. There are four main experiments located in the interaction points of the LHC, these are the CMS [26], the ATLAS [27], the LHCb [28] and the ALICE [29] experiments.

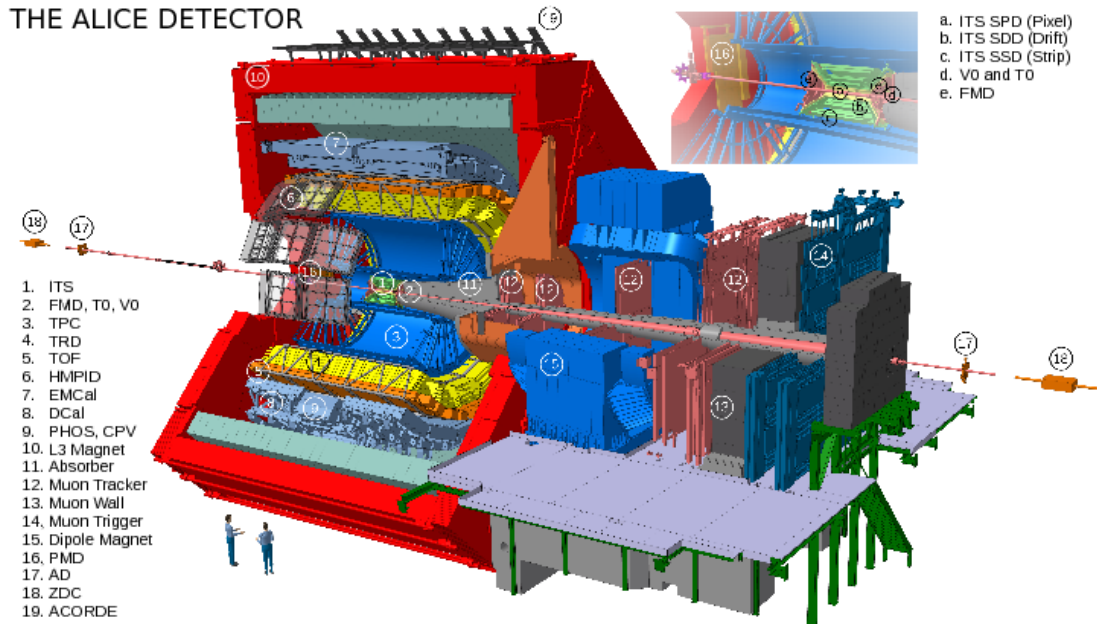


Figure 7: The structure of the ALICE detector system [29].

The ALICE experiment was designed in the early '90s and it recorded data from the first Pb-Pb collisions at the LHC in 2010 [25]. The experiment was dedicated directly to study QGP produced in heavy-ion collisions and it has a similar structure to the other complex detector systems. It is built up by different subdetectors and systems arranged into concentric layers surrounding the beam and the collision point. The detectors located inside in the inner layers are tracking detectors, calorimeters make up the most outer layers. The illustration of the ALICE detector can be found in the Fig. 7.

4.1 Tracking detectors

The Inner Tracking System (ITS) and the Time-Projection Chamber (TPC) are the two major tracking subsystems of the ALICE detector [30]. The ITS is located closest to the beam and its main purpose is the tracking and identification of charged particles with low transverse momentum ($|p_T| \leq 200 \text{ MeV}/c$) and takes part in the reconstruction of the primary and secondary vertices [30]. It consists of six layers of silicon detectors: the two innermost layers are Silicon Pixel Detectors (SPD), the two middle ones are Silicon Drift Detectors (SDD) and finally the two outermost layers are Silicon Strip Detectors (SSD). Furthermore, the detector is also part of the triggering system. The structure of the ITS is depicted in Fig. 8.

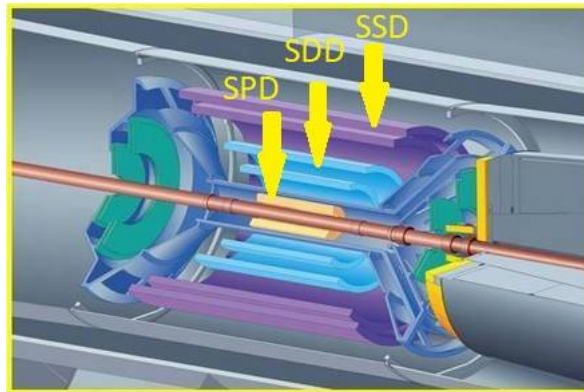


Figure 8: The structure of the Inner Tracking System (ITS) [31].

The next larger part of the tracking detector system is the TPC [32]. This has been optimised to be as sensitive as possible over a large momentum range. Currently, the ALICE experiment owns the world's largest MWPC-type TPC detector, with the sensitive volume of 88 m³. The advantage of gaseous detectors is that charged particles are scatter less in a lower density gas than in the semiconductors. Due to this reason, gaseous detectors allow more precise momentum resolution determination in low p_T than semiconductors. They are cost-efficient compared to silicon detectors, but gaseous detectors provide lower spatial resolution and they cannot handle as much luminosity as semiconductor detectors. The sensitivities of both the TPC and the ITS covers the full azimuthal range.

4.2 Particle identification

In ultra-relativistic heavy-ion collision measurements, it is essential to identify the particles with high efficiency. In the ALICE experiment there are dedicated subsystems for particle identification (PID). The main purpose of the Time-Of-Flight detector (TOF) is to distinguish pions, kaons, and protons based on the flight time between the detector and the vertex point. The reference time is determined by the T0 detector close. The next PID detector is the Transition Radiation Detector (TRD) which is used to identify mainly electrons above $p_T = 1$ GeV/ c . The last one is the High-Momentum Particle Identification Detector (HMPID) which is a Ring Imaging Cherenkov Radiation detector. Like the TRD it is also sensitive in the transverse momentum range above $p_T = 1$ GeV/ c . In addition to these tracking detectors are also used for PID purposes [32].

4.3 Electromagnetic Calorimeter

Calorimeters can usually can be found in the outer layers, since they measure the energy of the particles by the total absorption of them. Different calorimeters are used according to what particle we would like to detect: there are electromagnetic and hadronic calorimeters. The ALICE experiment has a main electromagnetic calorimeter (EMCal) which covers almost the half of the cylinder of the full azimuthal range ($\Delta\phi = 107^\circ$) and the pseudorapidity acceptance is $|\eta| < 0.7$ and besides that, two more calorimeters (PHOS and DCAL) can be found [30]. During the design of the EMCal the goal was to achieve the best possible energy resolution over a large range of p_T to a better study the particle showers.

4.4 Centrality measurements

Multiple detectors are used to measure the centrality. The V0 detector is built up of two parallel scintillation counters located on both side of the ITS. It measures the outgoing particles parallel to the beam in the pseudorapidity range of $2.8 < \eta < 5.1$ and $-3.7 < \eta < -1.7$. The detected particle yield is proportional to the generated multiplicity, from which the centrality can be determined. The Zero-Degree Calorimeter (ZDC) is also used to determine the centrality. It has two major parts, one neutron and one proton calorimeter which can be found on both sides of the interaction point at 115 meters away from the collision point (vvertex). These detectors completely surround the beam, and they are capable to measure the energy of the spectator particles of the collision, thereby the centrality can be calculated. We note that there are further detectors to determine the centrality.

5 Analysis method

As was previously mentioned in Sec. 2, jets are created in the early stage of the collisions and they interact with the formed quark-gluon plasma. Several tools have been developed to study these jets, since they provide useful information about the QCD medium. The most commonly used method is the full jet-reconstruction, e.g. the anti-Kt algorithm [33]. In these cases jets are reconstructed event-by-event from the particles detected in calorimeters and tracking detectors. Although, jet-reconstruction algorithms cannot be used when the transverse momenta of the partons are too low or the jet-quenching effect is too large [34, 35]. Due to this reason, another approach is when statistical average is taken over many events instead of event-by-event reconstruction. Thus the combinatorical background can be eliminated. Two particle angular-correlations belong to the second class of algorithms.

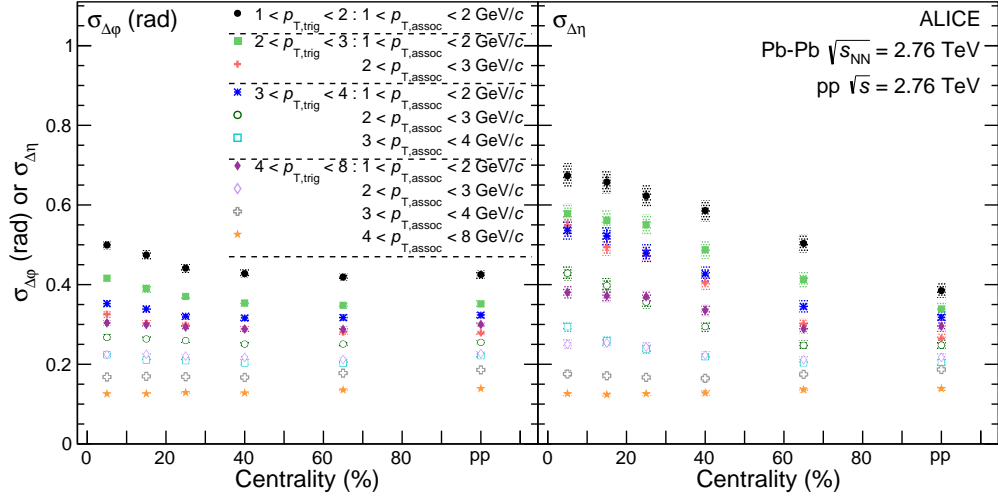


Figure 9: The widths of the near-side jet peak as the function of the centrality in Pb-Pb and pp collision with different p_T at $\sqrt{s_{NN}} = 2.76$ centre-of-mass energy per nucleon pair [36].

During the analysis, we examine the correlation of particles as a function of pseudorapidity ($\Delta\eta$) and azimuth angle ($\Delta\phi$) differences. In these correlations jets manifest themselves as a peak around ($\Delta\phi = 0, \Delta\eta = 0$) or as an elongated structure in $\Delta\phi$ around ($\Delta\phi = \pi$). The first one is called the near-side jet peak and the second one is usually referred to as away-side. As was have previously described in Sec. 2, the original volume, where QGP is formed strongly depends on the centrality. Because of this, the strength of the jet-energy loss correlates too with the centrality class. Two-particle angular correlations provide a powerful tool to study the centrality and p_T -dependence of the jet [37]. Unidentified angular correlation results from Pb-Pb collision taken by the ALICE experiment at $\sqrt{s_{NN}} = 2.76$ TeV centre-of-mass energy per nucleon per showed that in central collision, at low p_T the jet peaks are broadened and become asymmetrical. The width of the near-side jet peak as the function of the centrality and p_T has been depicted on Fig. 9, where it is clearly visible that the broadening is stronger in the $\Delta\eta$ than in the $\Delta\phi$ direction [36] and the broadening effect is stronger at low p_T . Furthermore, there is a depletion around $\Delta\phi = 0, \Delta\eta = 0$, in central collisions and at low p_T . An example of the depletion structure can be seen in Fig. 10. The authors in [36] suggested that the detailed observations (compared to AMPT simulations) are caused by the interplay of the jet with the collective expansion.

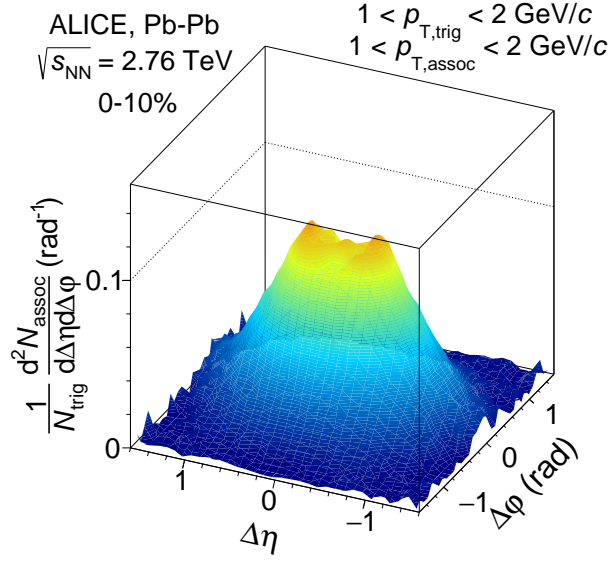


Figure 10: The depletion around $(\Delta\varphi = 0, \Delta\eta = 0)$ [36].

5.1 Two-particle angular correlations

In these measurements the correlation of particles is expressed as a function of $\Delta\varphi$ and $\Delta\eta$ differences between two chosen particles. The first particle is called trigger and the second is the associated particle. In the case of unidentified angular correlations there all charged particles are used for the trigger and associated particles. When the identified angular correlations is considered the trigger particles are exclusively pions (π^\pm), kaons (K^\pm) or protons (p^+). At the beginning of the analysis, the Pb-Pb events were sorted into different centrality and vertex classes. Then the particles are classified by their transverse momentum. Trigger and associated particles can be taken from different p_T classes, such that the $p_{T,trigger}$ class must be the higher one. When the $p_{T,trigger}$ and $p_{T,assoc}$ classes are equal. Only those differences are considered where $p_{T,trigger} > p_{T,assoc}$. Henceforward, the sensitive pseudorapidity and azimuthal ranges are divided into equal bins ($\delta\Delta\varphi = 0.062, \delta\Delta\eta = 0.032$) and then the number of hits detected in each bin is plotted. It is crucial, that histograms were filled separately according to their z -vertex classes to avoid effects arising from the different pair acceptance in each z -vertex class.

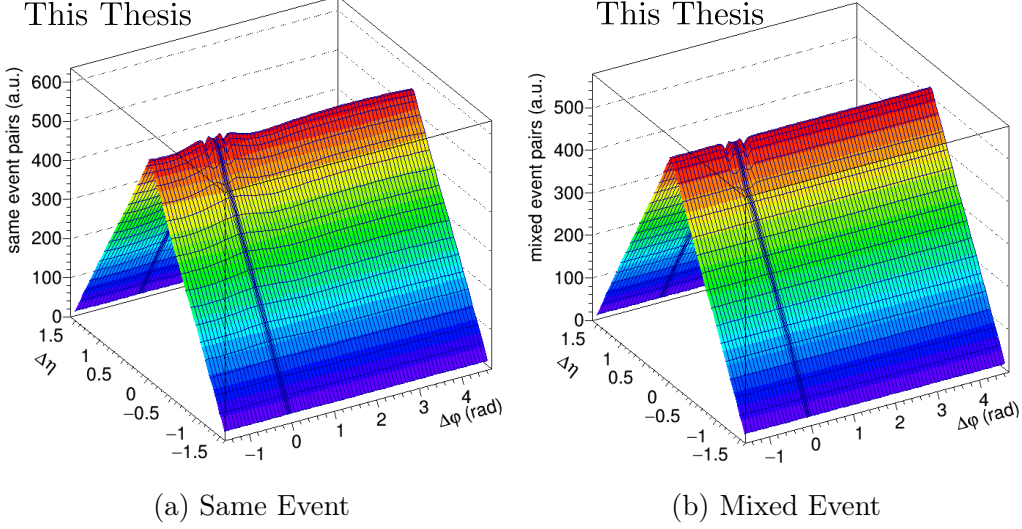


Figure 11: The example of a Same event (right) and a Mixed event (left) in Pb-Pb collision (30-40% cent.) at $\sqrt{s_{NN}} = 5.02$ TeV at low p_T limit: $1 \text{ GeV}/c \leq p_{T,trigger}, p_{T,assoc} \leq 2$.

This previously described distribution $S(\Delta\varphi, \Delta\eta)$ can occur in the following form:

$$S(\Delta\varphi, \Delta\eta) = \frac{d^2N}{d\Delta\varphi d\Delta\eta}. \quad (7)$$

This expression is commonly referred to as the Same event and is depicted in Fig. 11a. The dominant near-side jet peak is apparent in the picture around $\Delta\varphi = 0$, $\Delta\eta = 0$ and also a trivial triangular shape in $\Delta\eta$ can be observed. This effect comes from the fact that the detector has a finite acceptance in $|\eta| < 0.8$ and due to this reason a cut in $\Delta\eta$ was applied. This can be corrected by the mixed event technique, where the trigger and associated particles are used from different events. It means by definition, that the mixed event also contains the pair efficiency and finite acceptance effects but the physical correlations are not present. The histograms are filled separately for different p_T ranges, z -vertex and centrality bins in the same way as for same event and are shown in Fig. 11b. These events have been made from 5 to 20 events, depending on whether the centrality bin is considered. It is apparent in Fig. 11b that the structure has a maximum at $\Delta\eta = 0$ and it was be normalised by a factor, β so it is unity around $M(\Delta\varphi = 0, \Delta\eta = 0)$. The normalisation was taken from $\Delta\varphi = 0, \Delta\eta = 0$ because if the detector is perfect, the two particles with the same outgoing direction should have the same reconstruction efficiency. Instead of the value at the bin of $\Delta\varphi = 0, \Delta\eta = 0$ the average of four bins around it was used to reduce fluctuations. To conclude the form of the mixed distribution is

$$M(\Delta\varphi, \Delta\eta) = \frac{1}{\beta} \frac{d^2 N_{\text{mixed}}}{d\Delta\varphi d\Delta\eta} \quad (8)$$

In reality the detection is not perfect so there are small inefficiencies for which corrections are needed to be done. Those errors that originate from the track reconstruction inefficiencies or the contamination by secondary particles are corrected by a weight assigned to every detected particles depending on their pseudorapidity, z -vertex and p_T . For the determination of these weights Monte Carlo methods were used to simulate the interaction between particles and the detector material.

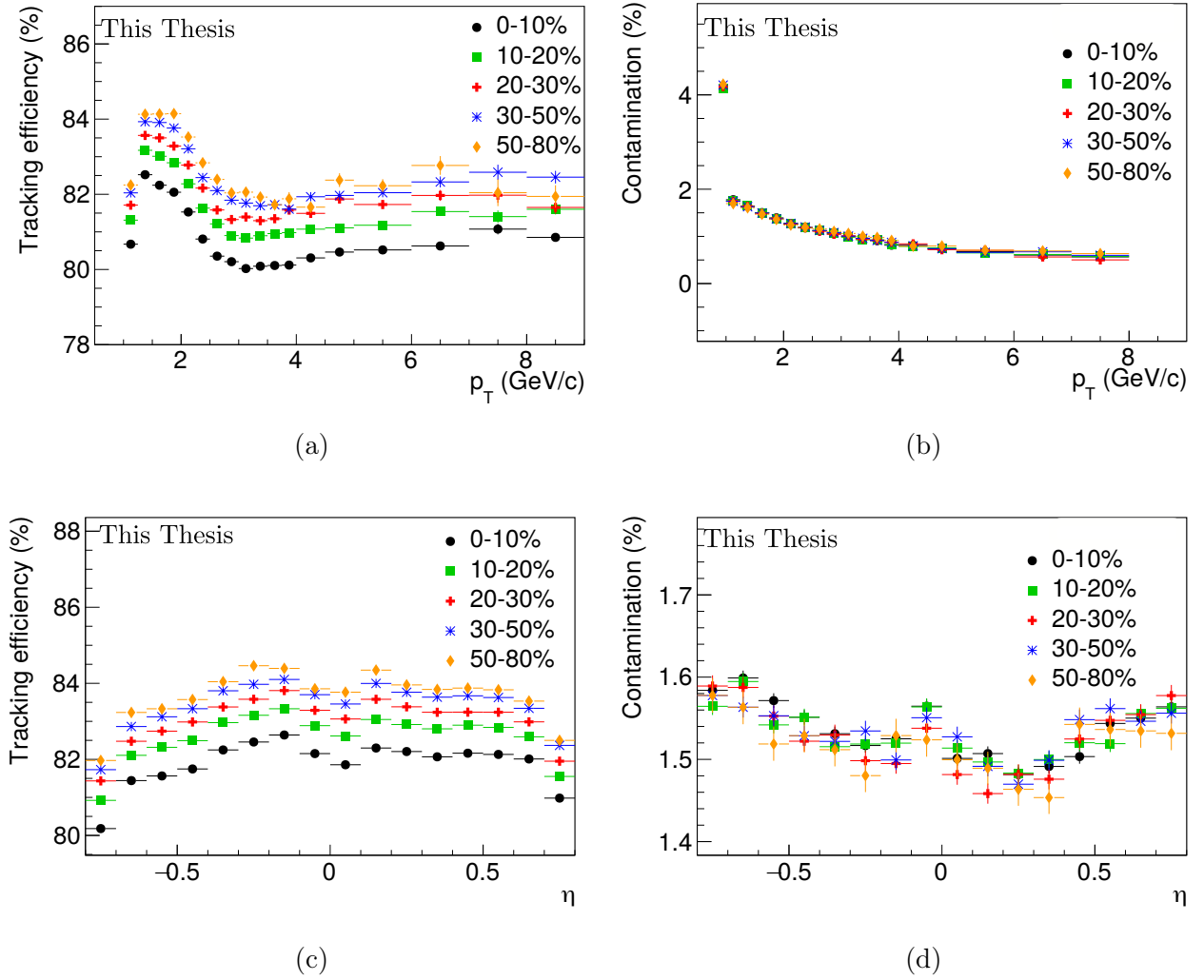


Figure 12: The results of the tracking efficiency and contamination as a function of p_T and η from Pb-Pb collision simulation using HIJING

Then the reconstruction was done for these simulated data the same way as for experimental data. Weights are calculated from the comparison of the MC simulated and reconstructed. Fig.12. shows the results of the tracking efficiency and contamination as a function of p_T and η . It is apparent that the tracking efficiency strongly depends on the transverse momentum and the pseudorapidity and there is small dependence on the centrality. The efficiency is higher if the collision is more peripheral and it can be seen that the contamination rises toward low p_T contrary to the efficiency which has a minimum at $p_T = 1$ GeV. After the efficiency and the contamination have been accounted for, the associated yield normalised by the number of triggers can be expressed as a sum of the same events divided by the mixed events from the different z -vertex bins:

$$\frac{1}{N_{trigger}} \frac{d^2 N_{assoc}}{d\Delta\varphi d\Delta\eta} = \frac{1}{N_{trigger}} \sum_i \frac{S_i(\Delta\varphi, \Delta\eta)}{M_i(\Delta\varphi, \Delta\eta)} \quad (9)$$

This has been depicted in Fig. 13. Two clear structures can be seen in the picture. The first one is the near-side jet peak around $(\Delta\varphi = 0, \Delta\eta = 0)$ and the second one is the cosine shape structure which is the azimuthal flow described in Section 2. Correlations of the decay products of Λ_0 and K_S^0 short-lived neutral particles are not studied in this analysis so they are removed by a cut on the invariant mass of the particle pairs. The same method was applied for the electrons and positrons originate from pair creation. It is commonly referred to as γ -conversion. In the measurements, an $\Delta\varphi$ -independent correlation occurs that originates from the η dependence of the particle creation and the elliptical flow. This can be removed by a division with the structure at $\Delta\varphi = \pi$.

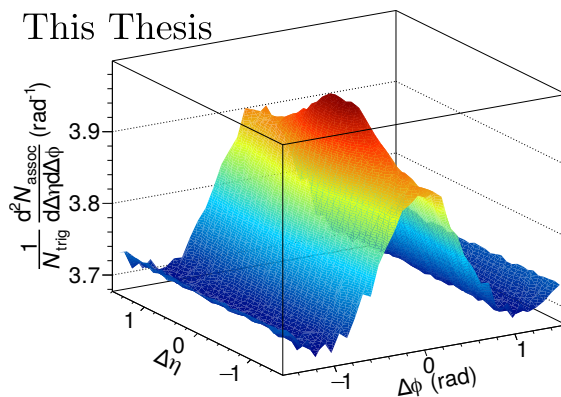


Figure 13: An example of the associated yield per trigger

The corrected associated yield per trigger is fitted with the method used in the ALICE experiment [37]. The fit has been made by a composite function of three parts. The first part is a generalised two-dimensional Gaussian, which (Eq. 10.) fits the near-side jet peak. The extra parameters ($\gamma_{\Delta\varphi}, \gamma_{\Delta\eta}$) are needed because the normal Gaussian-function does not fit well with the shape of the jet peak and fitting with the linear combination of two Gaussian functions was not stable. The second term in Eq. 11. is a Fourier series used to describe the azimuthal flow. The azimuthal flow in this case appears as a background for the near-side jet peak. The last part is a constant function ($C1$) which fits the combinatorial background.

$$G_{\gamma,\omega}(\Delta\varphi, \Delta\eta) = N \frac{\gamma_{\Delta\varphi}\gamma_{\Delta\eta}}{4\omega_{\Delta\varphi}\omega_{\Delta\eta}\Gamma(1/\gamma_{\Delta\varphi})\Gamma(1/\gamma_{\Delta\eta})} \exp \left[- \left(\frac{|\Delta\varphi|}{\omega_{\Delta\varphi}} \right)^{\gamma_{\Delta\varphi}} - \left(\frac{|\Delta\eta|}{\omega_{\Delta\eta}} \right)^{\gamma_{\Delta\eta}} \right] \quad (10)$$

$$F(\Delta\varphi, \Delta\eta) = C_1 + \sum_{n=2}^5 2V_{n\Delta} \cos(n\Delta\varphi) + C_2 G_{\gamma,\omega}(\Delta\varphi, \Delta\eta) \quad (11)$$

N is the normalisation parameter, the ω parameters represent the widths in different the two directions and the γ parameter describes the deviation from the standard Gaussian function. If $\gamma = 1$ we get a symmetric function with exponential decrease and if we choose $\gamma = 2$ we get back the standard Gaussian function. In the specific case when the γ parameter is larger than two we get a function like in the Fig. 14. With these parameters we can define a quantity which describes the width of the jet shape in both direction, this will be

$$\sigma_{\Delta\varphi;\Delta\eta} = \sqrt{\frac{\omega_{\Delta\varphi;\Delta\eta}^2 \Gamma(3/\gamma_{\Delta\varphi;\Delta\eta})}{\Gamma(1/\gamma_{\Delta\varphi;\Delta\eta})}} \quad (12)$$

The depletion yield is also calculated from the associated yield per trigger as in Ref. [37]. It cannot be determined directly from the fit. We used an excluded region around the centre of the peak where data points are not considered in the fitting process. The choice of the size of the excluded region is arbitrary, therefore the dependence of the yield from the region size has to be studied. It can be seen at Section. 5.4.5. There are a difference between the fitted peak and the data points. The depletion yield, by definition is determined by measuring this volume difference.

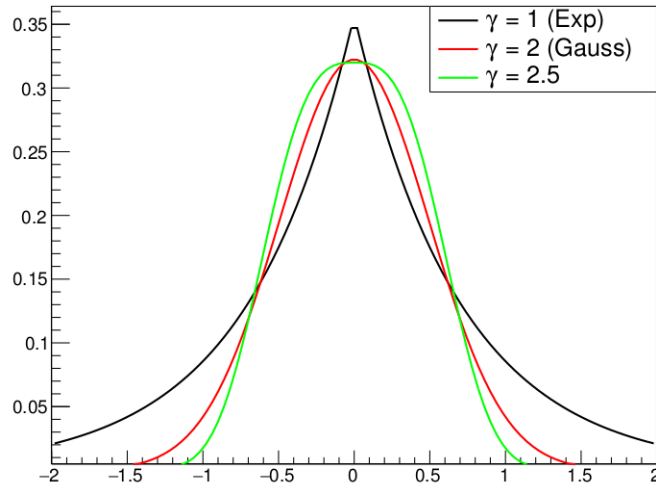


Figure 14: The shape of the generalised Gaussian, illustrated via different γ parameters.

5.2 Vertex and track reconstruction

The ITS and TPC detectors are used for vertex reconstruction. For the determination of the vertex point an extrapolation of the detected tracks are used. During this method the outlier tracks are removed and the vertex point is fitted after weighting the tracks [38]. The acceptance of the detector strongly depends on the z -position of the primary vertex, for this reason a limitation was introduced: in this analysis only those events were considered where the reconstructed vertex is within $\pm 7\text{cm}$ in the z -direction of the nominal collision point.

In this analysis, the so-called hybrid track reconstruction algorithms are used. This algorithm can be summarised as the following. For the track reconstruction, the TPC and ITS are used as well as for vertex reconstruction. However, the ITS had some inactive SPD modules during data taking, which causes a non-uniform acceptance in φ . This would result in the appearance of non-trivial structures as a function of $\Delta\varphi$, which could be a problem for angular correlation measurements. To avoid this effect, a set of tracks which have a hit in the SPD is combined with a set which do not have a hit in the SPD. It is true for all cases that these tracks are required to have at least 70 space points in the TPC and a $\chi^2/ndf < 2$ for the fit. In the second case, the primary vertex is used in constraining the tracks instead of the missing SPD hits. Detailed description can be found in [39].

5.3 Particle identification

In this analysis, the particle identification detectors from the inner barrel (ITS, TPC, TOF) were used. The mass of the particles are determined by their energy loss and the curvature of their track at the ITS and TPC and the time of flight measured by the TOF. The brief summary of the algorithm is the following: the detector response can be considered as an electric signal S . We presume that the detector response is Gaussian and let $\hat{S}(H_i)$ be the average detector response for a given particle species H_i then the σ_i the expected signal width. A statistical hypothesis test was made for every particle identification detector. Let us suppose that n_σ is the test function, which measure the deviation between the detected and the expected signal for every particle species H_i .

$$n_{\sigma_\alpha^i} = \frac{S_\alpha - \hat{S}(H_i)}{\sigma_\alpha^i} \quad (13)$$

where α represents the specific detector. One can notice that the n_σ function strongly depends on the specific particle and detector type. Finally, we assign a specific particle type for every track if the value of n_σ is below a certain limit [40]. In this analysis, I chosed this value as $n_\sigma < 3$ for all types of species. At below $p_T < 3 - 4$ GeV the track-by-track separation of hadrons made by the combination of PID signals from different detectors. The particle identification for particles with higher momenta was made by a statistical unfolding on the PID signals from the TPC [30].

5.4 Systematic uncertainties

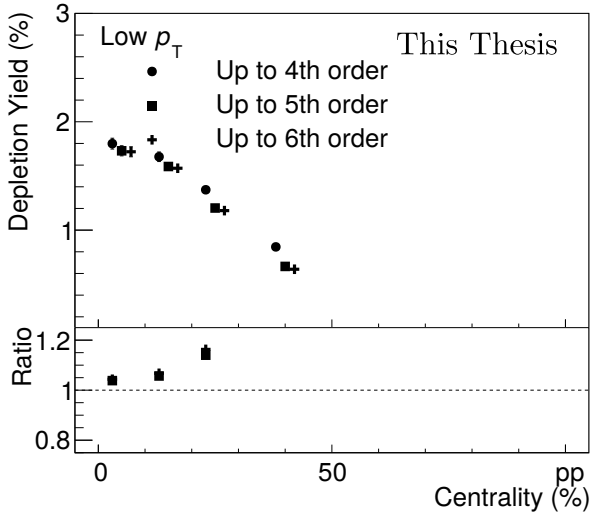
The systematic uncertainties usually occur by the consequences of observational error, imperfect instrument calibration, and any kind of environmental interference. In such analyses, where statistical methods are frequently used, it is essential to identify the origin and magnitude of systematic uncertainties. The nature of these uncertainties can be various and their determination is not trivial. In this section I will present the source of the systematic uncertainties and they are summarised below in Tab. 1. These particular errors are described in more detail in the following sections. Based on previous measurements [37], we expect that the depletion yield at high p_T is equal to zero. Therefore, the systematic uncertainties studied only at low p_T region for the depletion yield.

	Unidentified			Pion			Kaon		
	$\sigma_{\Delta\varphi}$	$\sigma_{\Delta\eta}$	Depletion	$\sigma_{\Delta\varphi}$	$\sigma_{\Delta\eta}$	Depletion	$\sigma_{\Delta\varphi}$	$\sigma_{\Delta\eta}$	Depletion
Background fit	0%	1%	5%	0%	1%	0%	0%	1%	10%
Magnetic field	0%	1.5%	5.5%	0%	1.2%	0%	0%	1.7%	20%
Pseudorapidity	0%	1.7%	5%	0%	2%	0%	1%	2.5%	20%
Vertex distance	0%	1%	3%	0%	1%	3%	0%	1%	3%
Excluded Region	0%	1%	5%	0%	1%	0%	0%	1%	7%

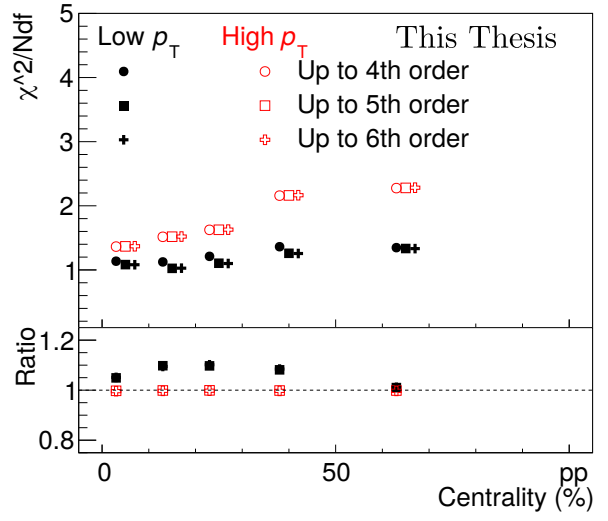
Table 1: The summary of the systematic uncertainties.

5.4.1 Background characterisation

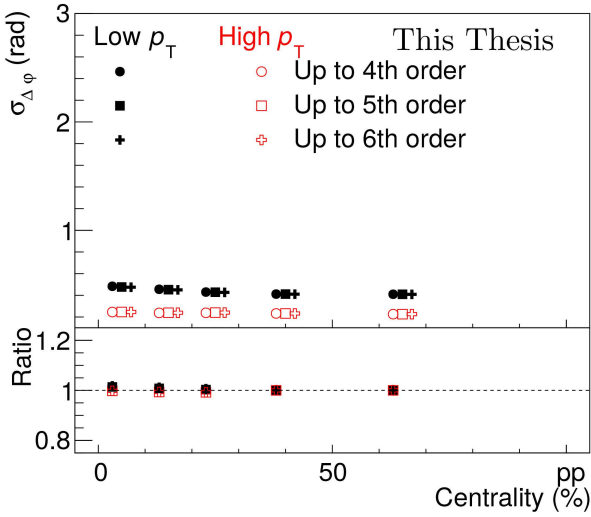
It is necessary to determine if the azimuthal flow can be described well with a background fit up to v_4 or higher order terms should be considered. Therefore, the χ^2/ndf , the depletion yield, and the widths in $\Delta\eta$ and $\Delta\varphi$ were determined and compared for different background fits up to 4^{th} , 5^{th} , 6^{th} orders. In the next step we will calculate the ratio between the results obtained by the fit up to 4^{th} and results from fits with additional flow parameters. These ratios have been depicted on every following figures and these were used for the estimation of the systematic uncertainties. Fig. 15. shows that there is a significant difference between the fits of 4^{th} , 5^{th} orders. The deviation between the 5^{th} and 6^{th} orders is less than 5%. Due to this reason, the v_6 can be neglected hereinafter and v_5 will be the last term considered. One can notice, that there are only one error on Fig. 15., that is because the depletion yield was equal to zero in case of identified angular correlations. Figs 17a. and 15a. shows that the errors of the depletion yield have a clear centrality dependence.



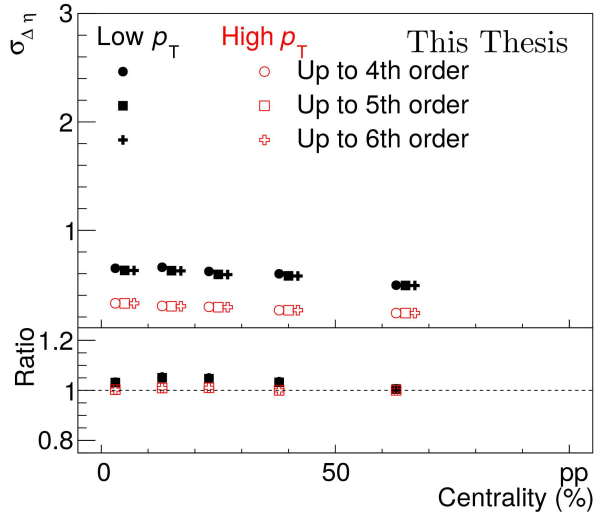
(a)



(b)

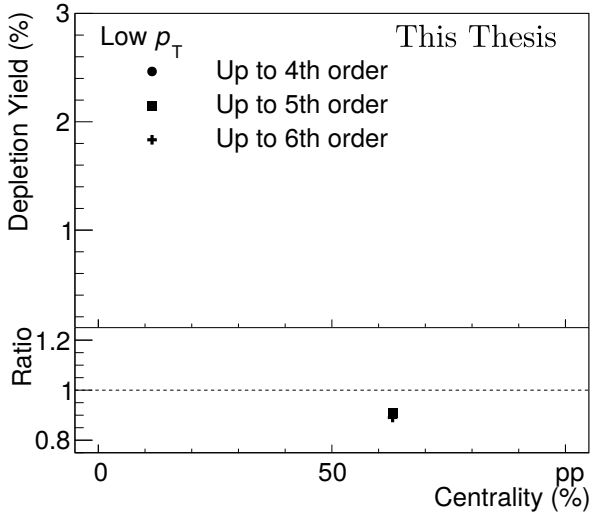


(c)

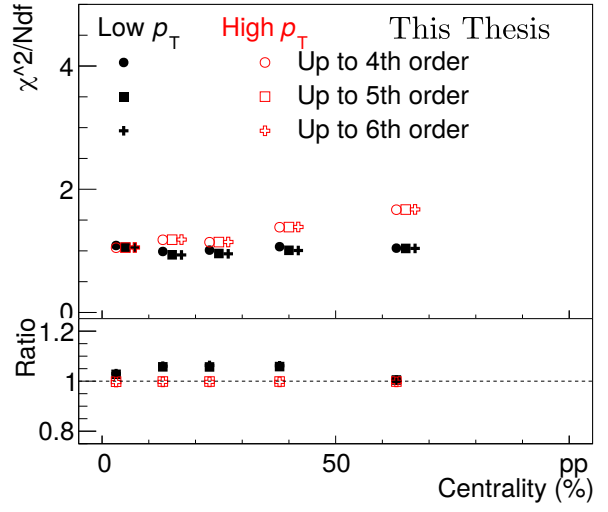


(d)

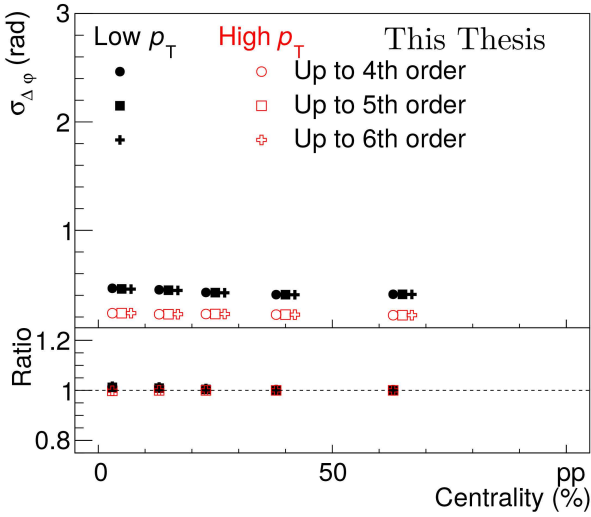
Figure 15: The background fits up to different orders: χ^2/ndf (a), depletion yield (b) and $\sigma_{\Delta\eta}$ (c) and $\sigma_{\Delta\phi}$ (d) widths at low p_T : $1 \text{ GeV}/c \leq p_{T,trigger}, p_{T,assoc} \leq 2 \text{ GeV}/c$ and at high p_T : $4 \text{ GeV}/c \leq p_{T,trigger} \leq 8 \text{ GeV}/c$ and $2 \text{ GeV}/c \leq p_{T,assoc} \leq 3 \text{ GeV}/c$. (for unidentified particles)



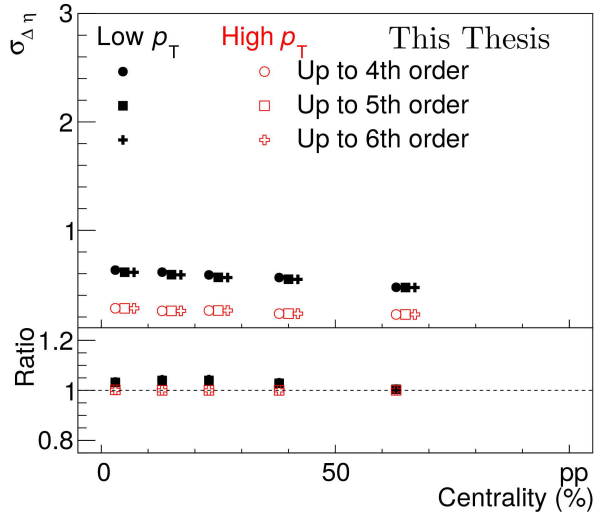
(a)



(b)

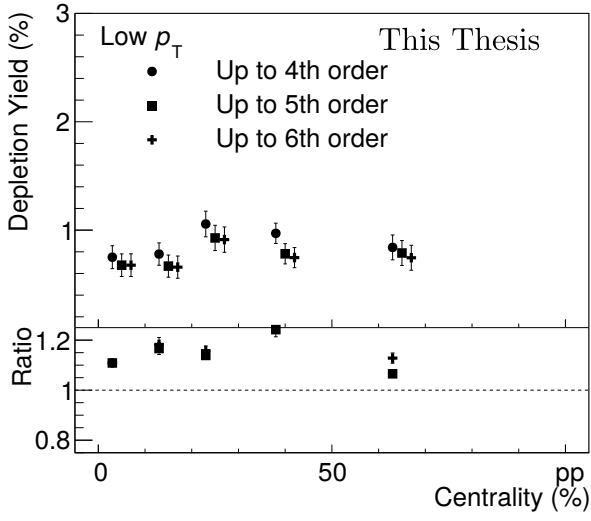


(c)

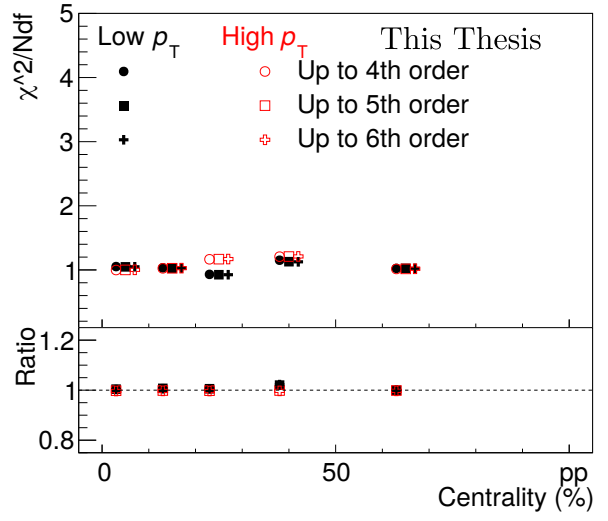


(d)

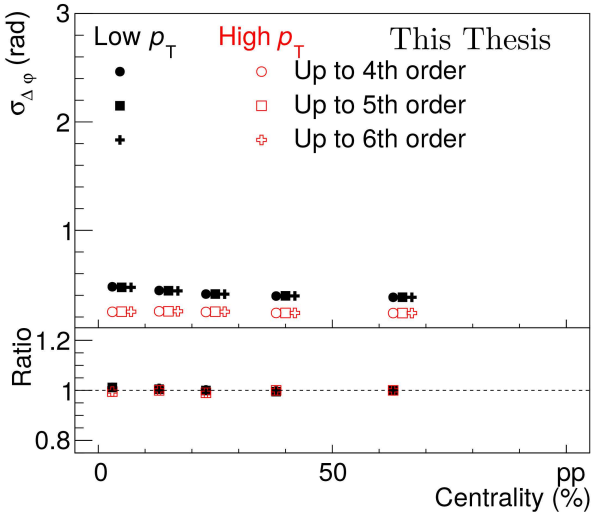
Figure 16: The background fits up to different orders: χ^2/ndf (a), depletion yield (b) and $\sigma_{\Delta\eta}$ (c) and $\sigma_{\Delta\phi}$ (d) widths at low p_T : $1 \text{ GeV}/c \leq p_{T,trigger}, p_{T,assoc} \leq 2 \text{ GeV}/c$ and at high p_T : $4 \text{ GeV}/c \leq p_{T,trigger} \leq 8 \text{ GeV}/c$ and $2 \text{ GeV}/c \leq p_{T,assoc} \leq 3 \text{ GeV}/c$. (for identified kaon)



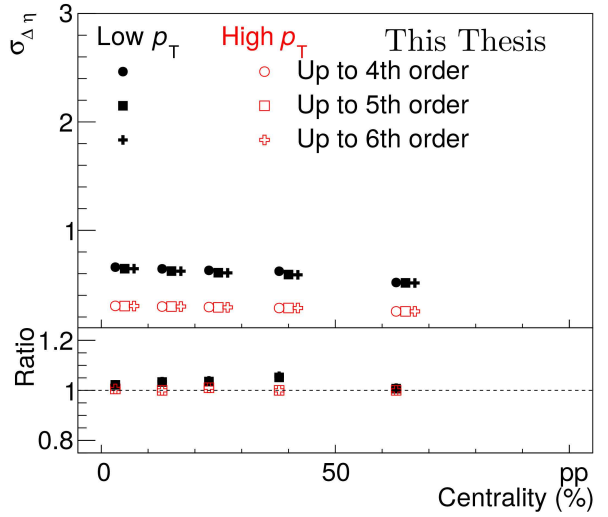
(a)



(b)



(c)



(d)

Figure 17: The background fits up to different orders: χ^2/ndf (a), depletion yield (b) and $\sigma_{\Delta\eta}$ (c) and $\sigma_{\Delta\phi}$ (d) widths at low p_T : $1 \text{ GeV}/c \leq p_{T,trigger}, p_{T,assoc} \leq 2 \text{ GeV}/c$ and at high p_T : $4 \text{ GeV}/c \leq p_{T,trigger} \leq 8 \text{ GeV}/c$ and $2 \text{ GeV}/c \leq p_{T,assoc} \leq 3 \text{ GeV}/c$. (for identified kaon)

5.4.2 The effect of the magnetic field

At the ALICE experiment a 0.5 T dipole magnetic field are used for the measurement of the transverse momenta of all charged particle. In the measurements both positive and negative magnetic field configuration are used. The direction of curvature of the charged particle tracks will differ based on the magnetic configuration setup. Thereby they can affect the obtained results [22]. During the analysis, data recorded under different configurations are stored separately and were unified directly before the division and the second when it is done after the division by the mixed event. The uncertainties are obtained by the comparison of two cases, the first one is where the unification happens before the division. These results are depicted in Fig. 18, for unidentified hadron-hadron correlations, in Fig. 19 for identified pion-hadron correlations and finally in Fig. 20 for identified kaon-hadron correlations. We can conclude from the ratios, that the systematic errors for the near-side jet-peak is below than 1% and 2% in direction of $\Delta\varphi$ and $\Delta\eta$ respectively. There are no errors on Fig. 19a., because there was no depletion structure in case of the identified pion correlation. Although, if we look at the case of depletion yield from the other two cases, we can summarise that there is a significant error which is equal to 5% and 20% respectively.

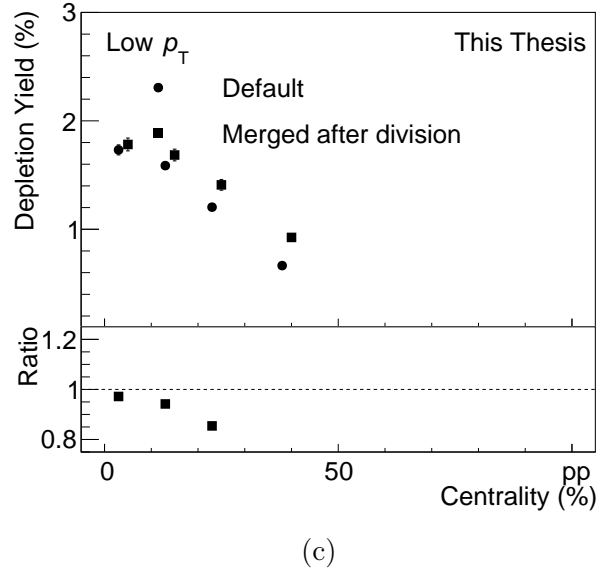
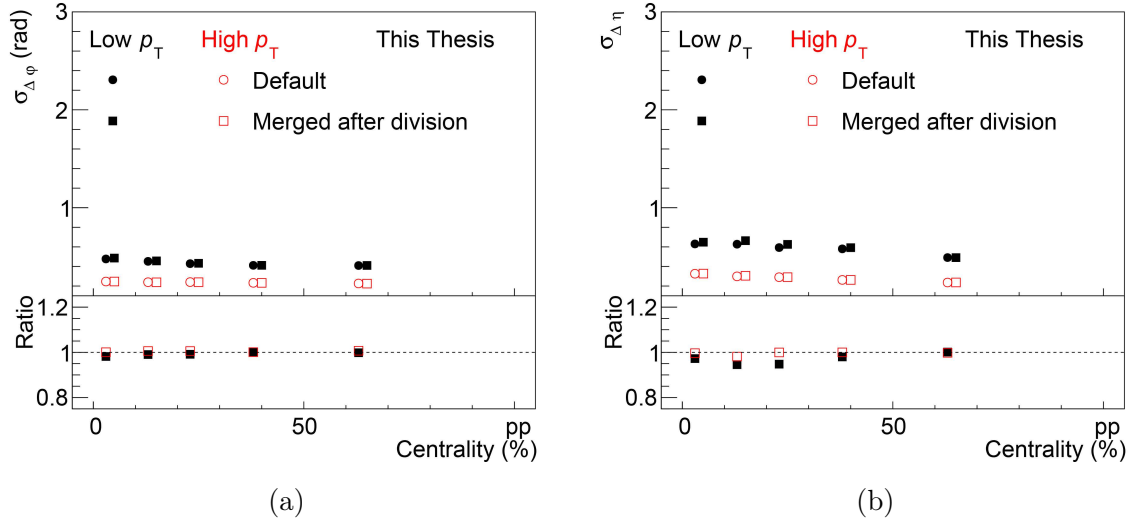
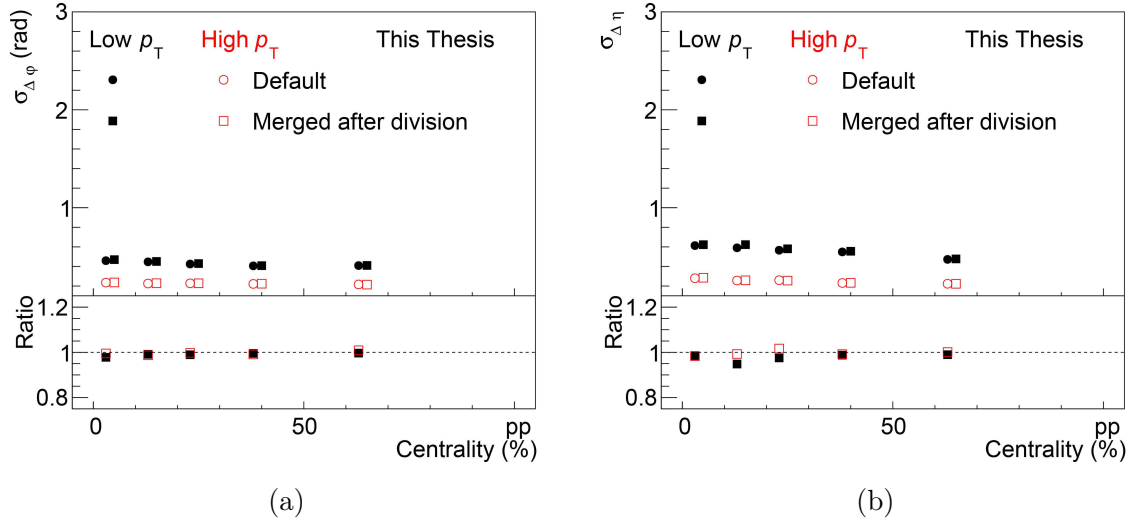
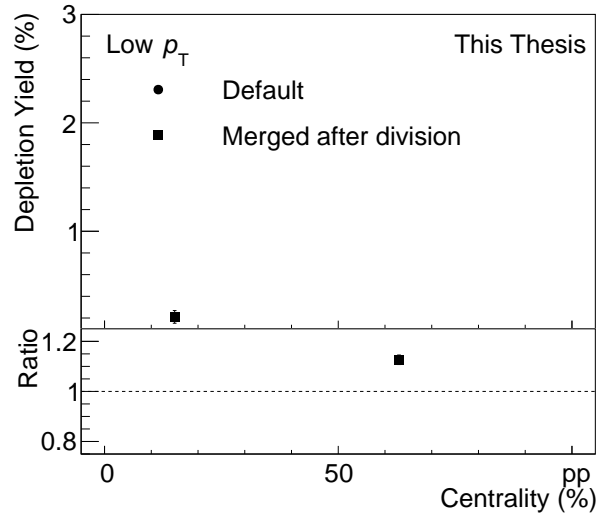


Figure 18: Generalised Gaussian fits with different magnetic configuration: depletion yield (c) and $\sigma_{\Delta\eta}$ (b) and $\sigma_{\Delta\phi}$ (a) widths at low p_T : $1 \text{ GeV}/c \leq p_{T,trigger}, p_{T,assoc} \leq 2 \text{ GeV}/c$ and at high p_T : $4 \text{ GeV}/c \leq p_{T,trigger} \leq 8 \text{ GeV}/c$ and $2 \text{ GeV}/c \leq p_{T,assoc} \leq 3 \text{ GeV}/c$. (for unidentified particles)



(a)

(b)



(c)

Figure 19: Generalised Gaussian fits with different magnetic configuration: depletion yield (c) and $\sigma_{\Delta\eta}$ (b) and $\sigma_{\Delta\phi}$ (a) widths at low p_T : $1 \text{ GeV}/c \leq p_{T,trigger}, p_{T,assoc} \leq 2 \text{ GeV}/c$ and at high p_T : $4 \text{ GeV}/c \leq p_{T,trigger} \leq 8 \text{ GeV}/c$ and $2 \text{ GeV}/c \leq p_{T,assoc} \leq 3 \text{ GeV}/c$. (for identified pion)

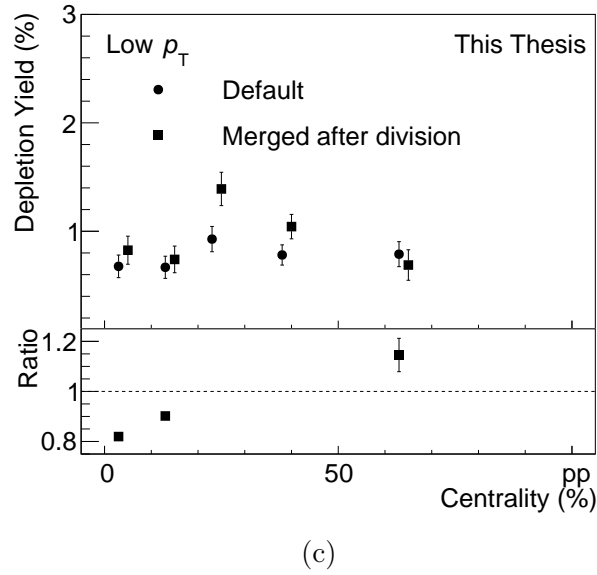
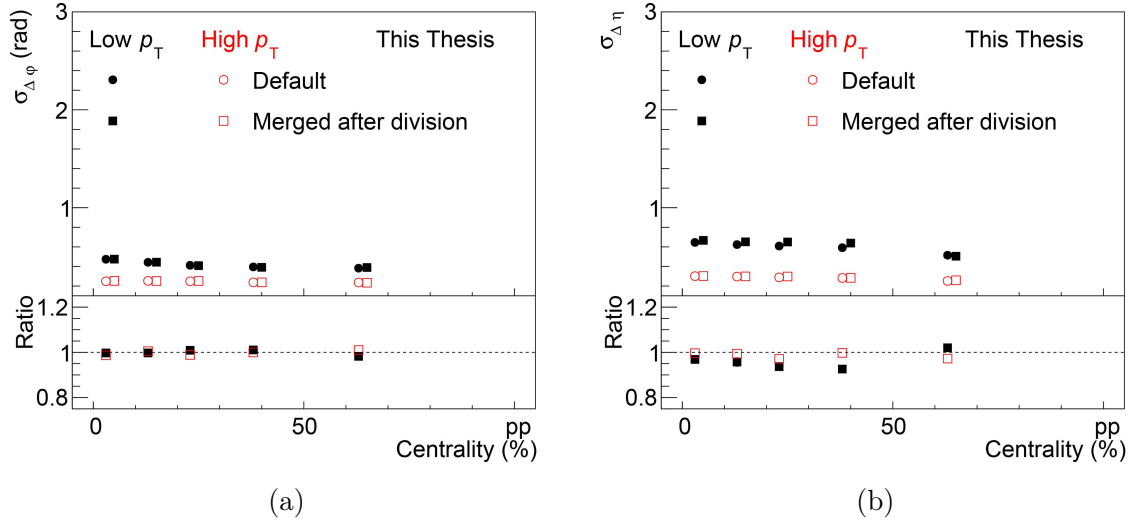


Figure 20: Generalised Gaussian fits with different magnetic configuration: depletion yield (c) and $\sigma_{\Delta\eta}$ (b) and $\sigma_{\Delta\phi}$ (a) widths at low p_T : $1 \text{ GeV}/c \leq p_{T,trigger}, p_{T,assoc} \leq 2 \text{ GeV}/c$ and at high p_T : $4 \text{ GeV}/c \leq p_{T,trigger} \leq 8 \text{ GeV}/c$ and $2 \text{ GeV}/c \leq p_{T,assoc} \leq 3 \text{ GeV}/c$. (for identified kaon)

5.4.3 Pseudorapidity dependence

In this analysis a pseudorapidity cut of $|\eta| < 0.8$ is used. However, the associated yield per trigger can depend on the chosen pseudorapidity limit. For this reason, I studied those cases, where the pseudorapidity cuts are equal to $|\eta| < 0.7$ or $|\eta| < 0.9$ and after that I compared the obtained results to each other. It can be seen in Figs. 21, 22 and 23. that there are differences between the obtained depletion yields and near-side jet peak widths. The ratios between the $|\eta| < 0.7$ results and the other cases show that systematic uncertainties are smaller than 1% and 2% for the cases of $\sigma_{\Delta\varphi}$ and $\sigma_{\Delta\eta}$ respectively. The deviation between the depletion yield is much more significant and has a strong centrality dependence. The errors were estimated to 5% for the unidentified particles and 20% in case of kaon-hadron correlations. To summarise these results, in the analysis we used the $|\eta| < 0.8$ cutoff.

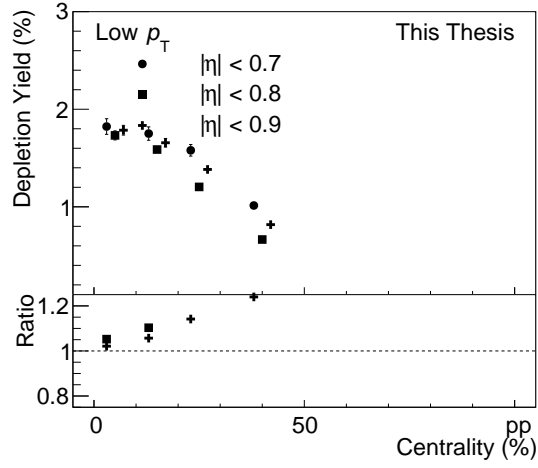
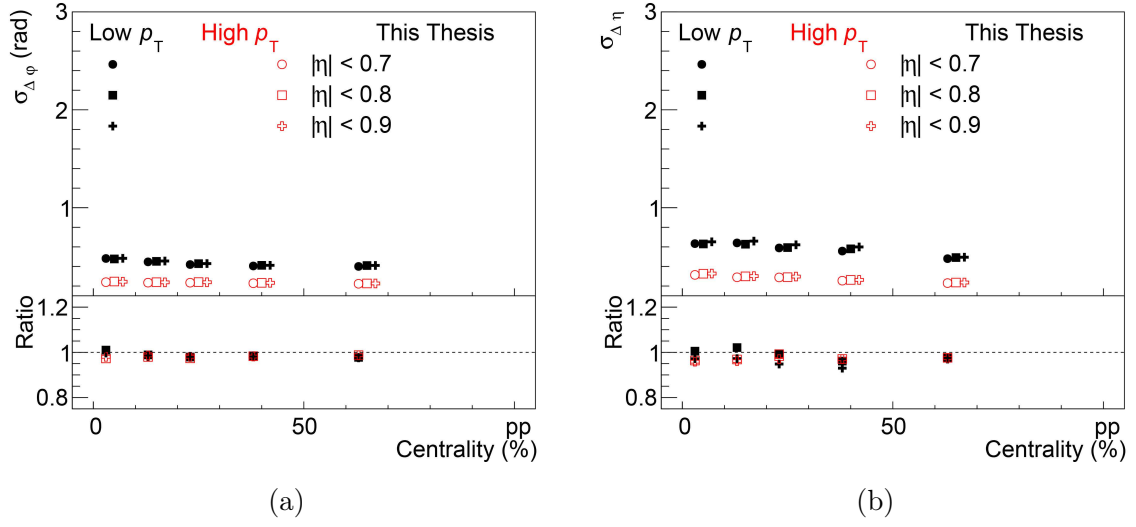


Figure 21: Generalised Gaussian fit results as the function of $|\eta|$ cutoff: depletion yield (c) and $\sigma_{\Delta\eta}$ (b) and $\sigma_{\Delta\phi}$ (a) widths at low p_T : $1 \text{ GeV}/c \leq p_{T,trigger}, p_{T,assoc} \leq 2 \text{ GeV}/c$ and at high p_T : $4 \text{ GeV}/c \leq p_{T,trigger} \leq 8 \text{ GeV}/c$ and $2 \text{ GeV}/c \leq p_{T,assoc} \leq 3 \text{ GeV}/c$. (for unidentified particles)

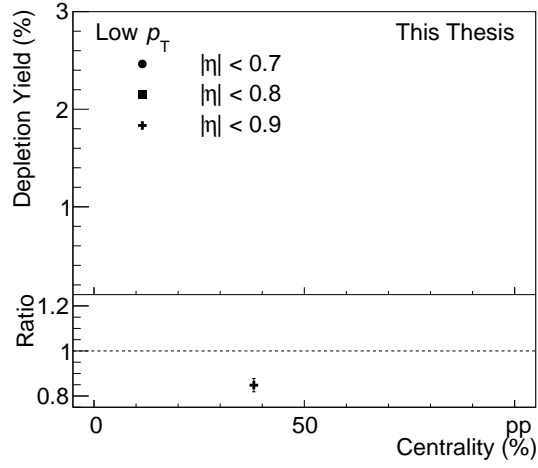
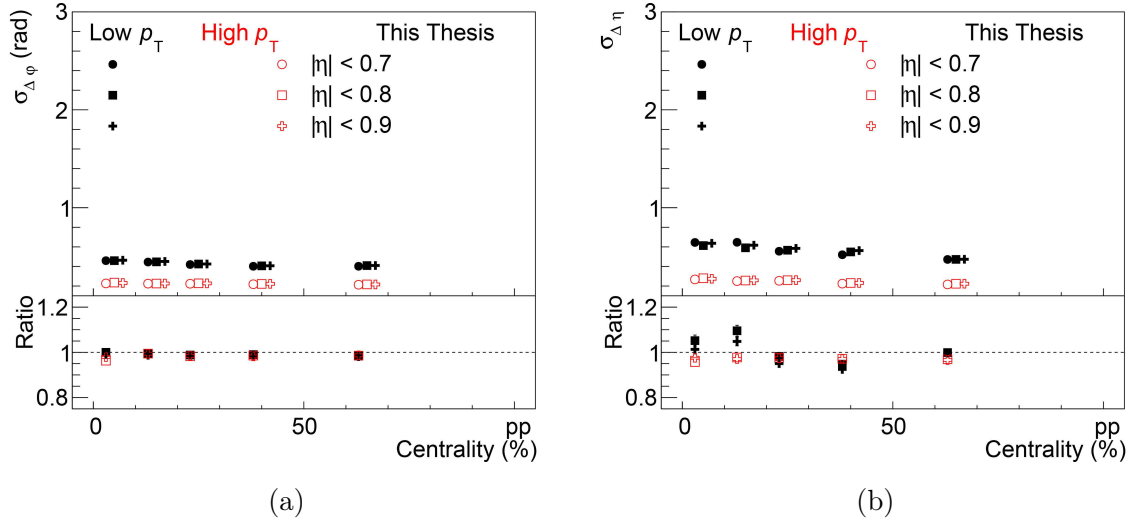


Figure 22: Generalised Gaussian fit results as the function of $|\eta|$ cutoff: depletion yield (c) and $\sigma_{\Delta\eta}$ (b) and $\sigma_{\Delta\phi}$ (a) widths at low p_T : $1 \text{ GeV}/c \leq p_{T,trigger}, p_{T,assoc} \leq 2 \text{ GeV}/c$ and at high p_T : $4 \text{ GeV}/c \leq p_{T,trigger} \leq 8 \text{ GeV}/c$ and $2 \text{ GeV}/c \leq p_{T,assoc} \leq 3 \text{ GeV}/c$. (for identified pion)

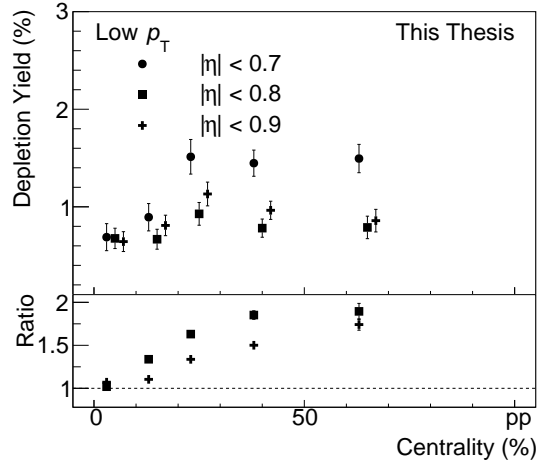
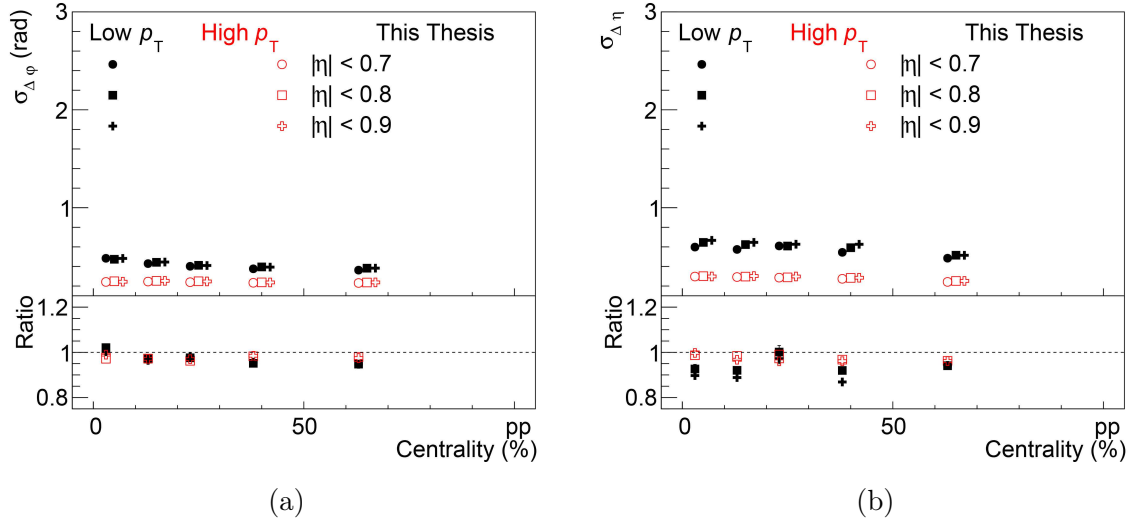


Figure 23: Generalised Gaussian fit results as the function of $|\eta|$ cutoff: depletion yield (c) and $\sigma_{\Delta\eta}$ (b) and $\sigma_{\Delta\phi}$ (a) widths at low p_T : $1 \text{ GeV}/c \leq p_{T,trigger}, p_{T,assoc} \leq 2 \text{ GeV}/c$ and at high p_T : $4 \text{ GeV}/c \leq p_{T,trigger} \leq 8 \text{ GeV}/c$ and $2 \text{ GeV}/c \leq p_{T,assoc} \leq 3 \text{ GeV}/c$. (for identified kaon)

5.4.4 Vertex range

In angular correlation analyses only those events were considered where the reconstructed vertices are within ± 7 centimeters of the detector's geometric centre in the direction of the beam. The η and $\Delta\eta$ distribution changes with the position of the z -vertex, for this reason we study the effect of changing its value to ± 3 centimetre. Figs. 24. and 25 show the obtained results of the depletion yield and the widths as a function of the z -vertex range and p_T . The results show that there is no large difference between the obtained widths in $\Delta\eta$ or in $\Delta\varphi$, but there is a large difference in case of the depletion yield. Figs. 26., 28., 27 and 29 demonstrates that the identified cases shows similar trends as like the unidentified case.

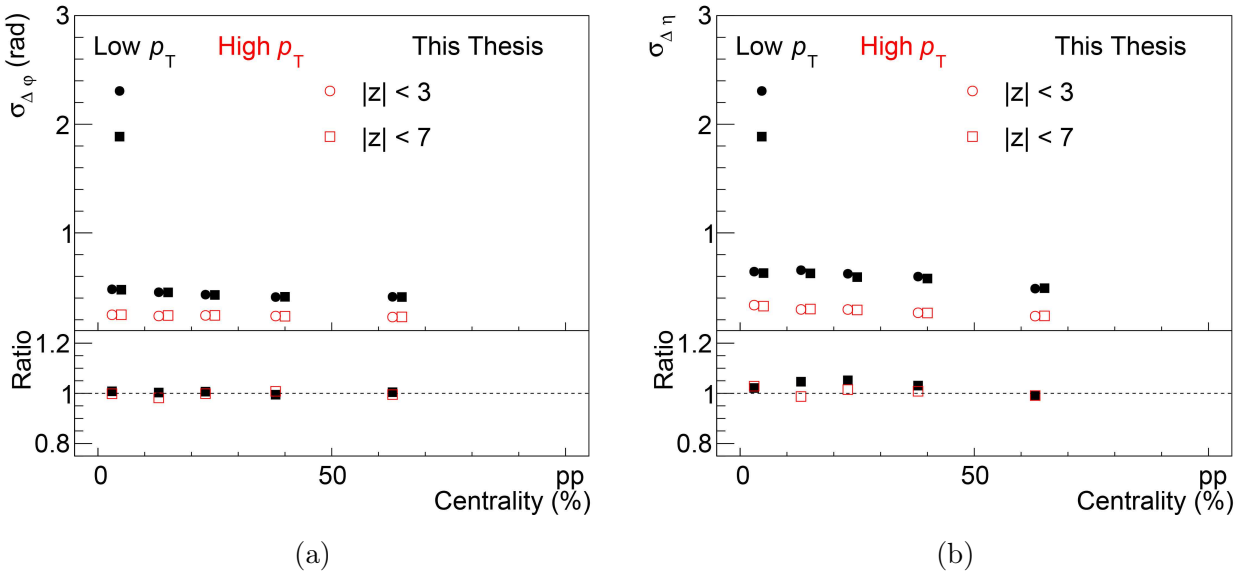


Figure 24: Generalised Gaussian fit results as the function of z -vertex range: $\sigma_{\Delta\eta}$ (b) and $\sigma_{\Delta\varphi}$ (a) widths at low p_T : $1 \text{ GeV}/c \leq p_{T,trigger}, p_{T,assoc} \leq 2 \text{ GeV}/c$ and at high p_T : $4 \text{ GeV}/c \leq p_{T,trigger} \leq 8 \text{ GeV}/c$ and $2 \text{ GeV}/c \leq p_{T,assoc} \leq 3 \text{ GeV}/c$. (for unidentified particles)

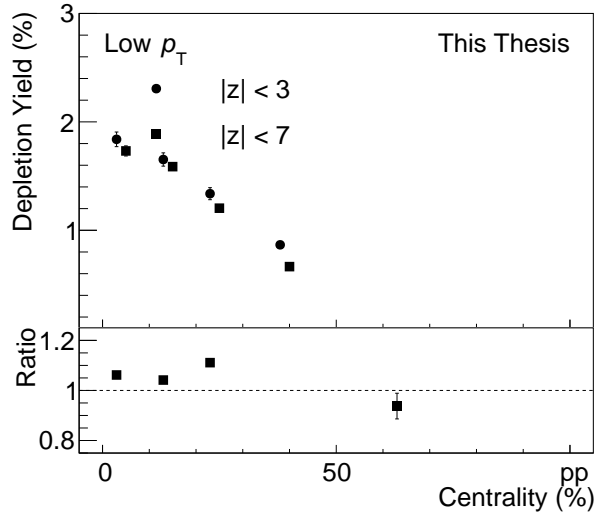


Figure 25: Depletion yield results as the function of z -vertex range at low p_T : $1 \text{ GeV}/c \leq p_{T,trigger}, p_{T,assoc} \leq 2 \text{ GeV}/c$ and at high p_T : $4 \text{ GeV}/c \leq p_{T,trigger} \leq 8 \text{ GeV}/c$ and $2 \text{ GeV}/c \leq p_{T,assoc} \leq 3 \text{ GeV}/c$. (for unidentified particles)

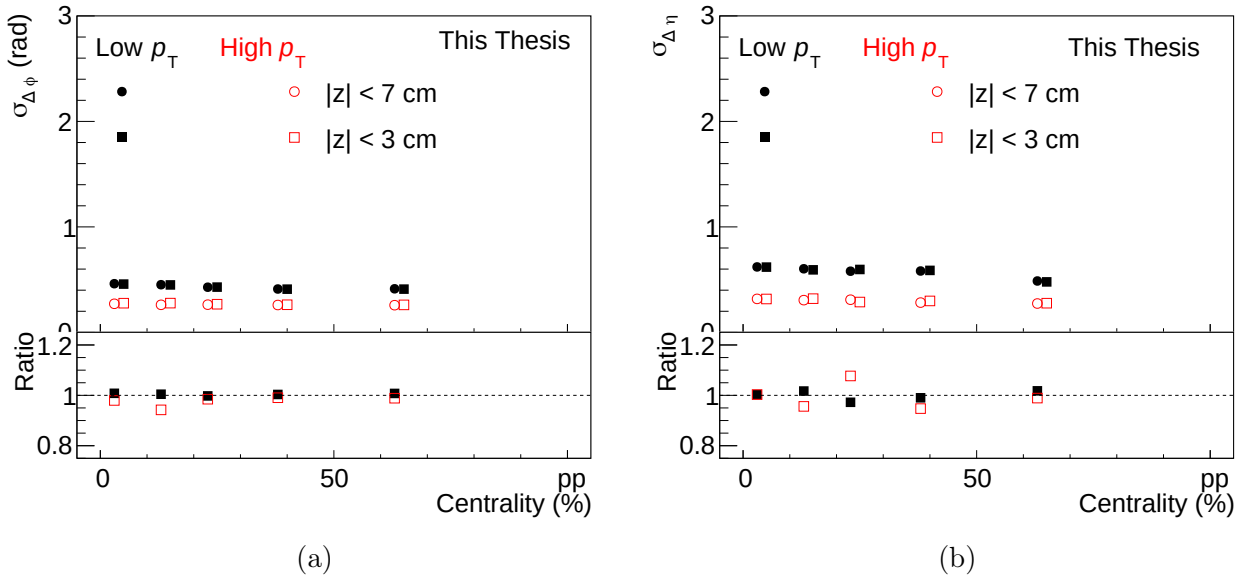


Figure 26: Generalised Gaussian fit results as the function of z -vertex range: $\sigma_{\Delta\eta}$ (b) and $\sigma_{\Delta\phi}$ (a) widths at low p_T : $1 \text{ GeV}/c \leq p_{T,trigger}, p_{T,assoc} \leq 2 \text{ GeV}/c$ and at high p_T : $4 \text{ GeV}/c \leq p_{T,trigger} \leq 8 \text{ GeV}/c$ and $2 \text{ GeV}/c \leq p_{T,assoc} \leq 3 \text{ GeV}/c$. (for identified pion)

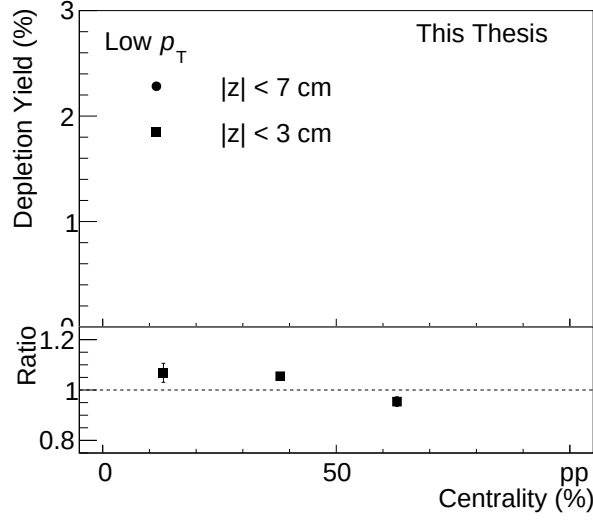
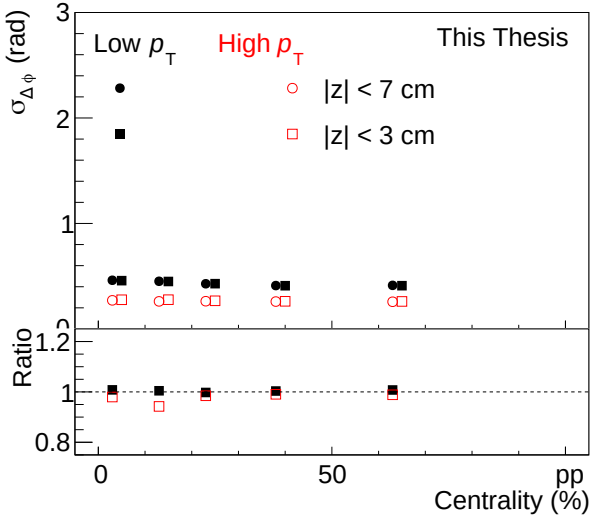
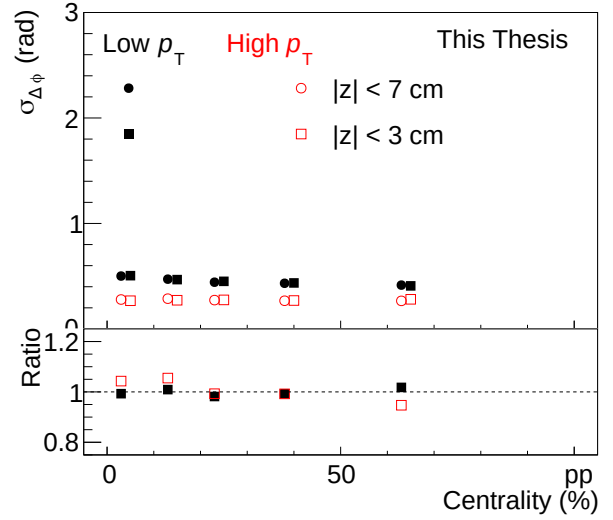


Figure 27: Depletion yield results as the function of z -vertex range at low p_T : $1 \text{ GeV}/c \leq p_{T,trigger}, p_{T,assoc} \leq 2 \text{ GeV}/c$ and at high p_T : $4 \text{ GeV}/c \leq p_{T,trigger} \leq 8 \text{ GeV}/c$ and $2 \text{ GeV}/c \leq p_{T,assoc} \leq 3 \text{ GeV}/c$. (for identified pion)



(a)



(b)

Figure 28: Generalised Gaussian fit results as the function of z -vertex range: $\sigma_{\Delta\eta}$ (b) and $\sigma_{\Delta\phi}$ (a) widths at low p_T : $1 \text{ GeV}/c \leq p_{T,trigger}, p_{T,assoc} \leq 2 \text{ GeV}/c$ and at high p_T : $4 \text{ GeV}/c \leq p_{T,trigger} \leq 8 \text{ GeV}/c$ and $2 \text{ GeV}/c \leq p_{T,assoc} \leq 3 \text{ GeV}/c$. (for identified kaon)

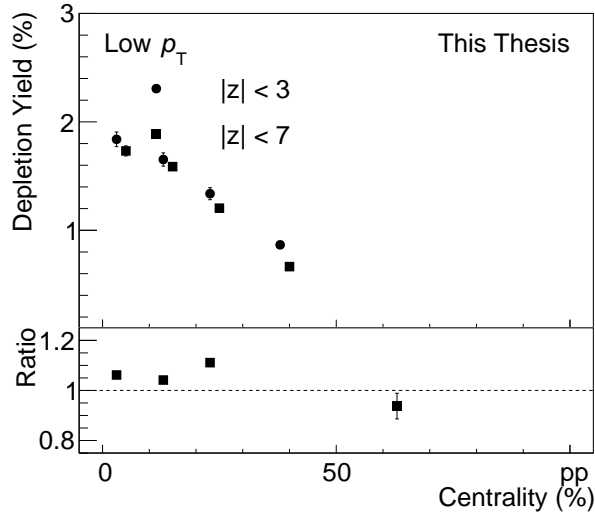


Figure 29: Depletion yield results as the function of z -vertex range at low p_T : $1 \text{ GeV}/c \leq p_{T,trigger}, p_{T,assoc} \leq 2 \text{ GeV}/c$ and at high p_T : $4 \text{ GeV}/c \leq p_{T,trigger} \leq 8 \text{ GeV}/c$ and $2 \text{ GeV}/c \leq p_{T,assoc} \leq 3 \text{ GeV}/c$. (for identified kaon)

5.4.5 Excluded Region

To determine the size of the depletion it is necessary to choose a size for the excluded region that will not be considered during the fit as it was described in Sec. 5.1. The size of the excluded region is arbitrary, for this reason systematic uncertainties are obtained by changing the size of this region. Figs. 30, 31 and 32 show the results for us. One can notice that the error for the measurement of the widths is less than 1.5% and the error for the depletion yield is approximately 10%.

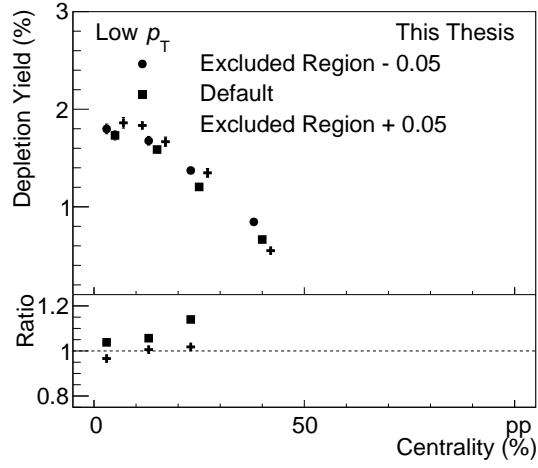
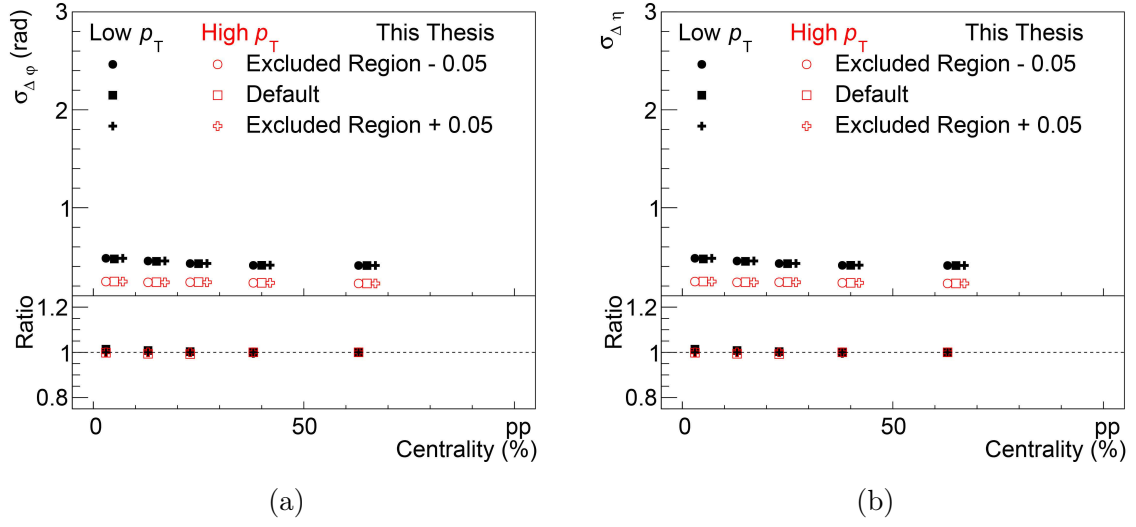


Figure 30: Generalised Gaussian fit results as the function of the size of the excluded region: depletion yield (a) and $\sigma_{\Delta\eta}$ (b) and $\sigma_{\Delta\phi}$ (c) widths at low p_T : $1 \text{ GeV}/c \leq p_{T,trigger}, p_{T,assoc} \leq 2 \text{ GeV}/c$ and at high p_T : $4 \text{ GeV}/c \leq p_{T,trigger} \leq 8 \text{ GeV}/c$ and $2 \text{ GeV}/c \leq p_{T,assoc} \leq 3 \text{ GeV}/c$. (for unidentified particles)

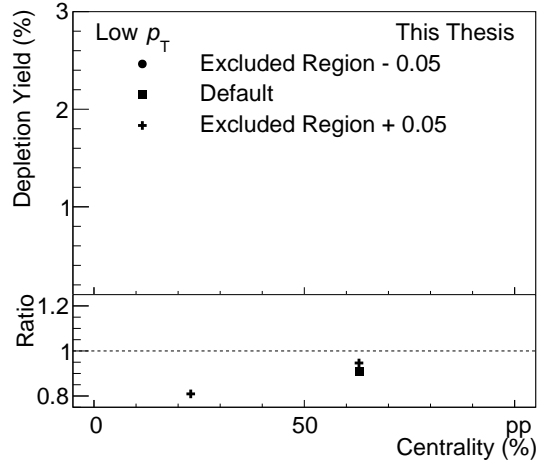
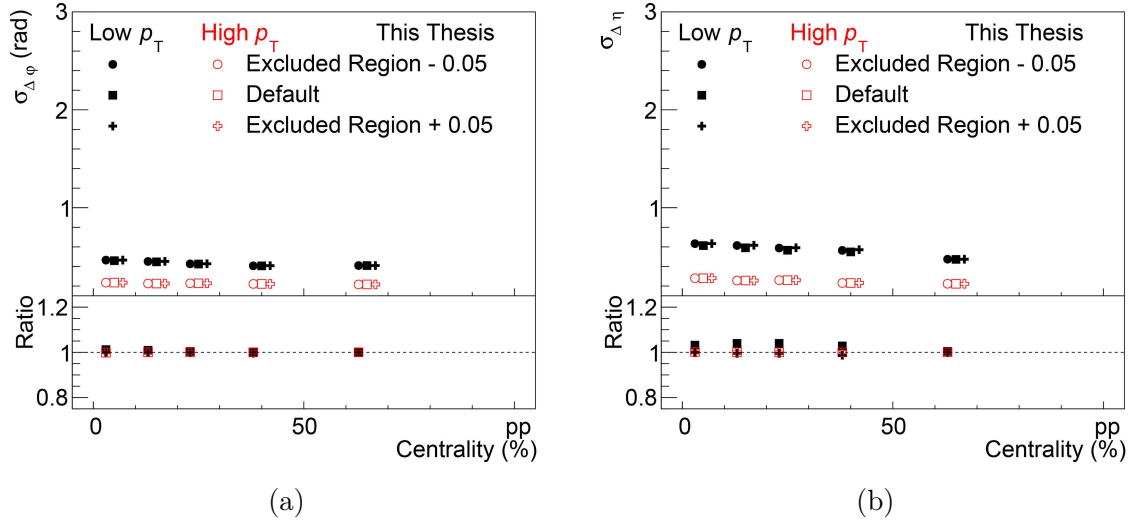


Figure 31: Generalised Gaussian fit results as the function of the size of the excluded region: depletion yield (a) and $\sigma_{\Delta\eta}$ (b) and $\sigma_{\Delta\phi}$ (c) widths at low p_T : $1 \text{ GeV}/c \leq p_{T,trigger}, p_{T,assoc} \leq 2 \text{ GeV}/c$ and at high p_T : $4 \text{ GeV}/c \leq p_{T,trigger} \leq 8 \text{ GeV}/c$ and $2 \text{ GeV}/c \leq p_{T,assoc} \leq 3 \text{ GeV}/c$. (for identified pion)

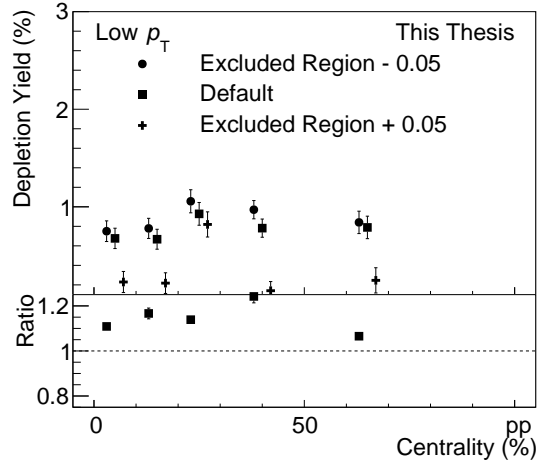
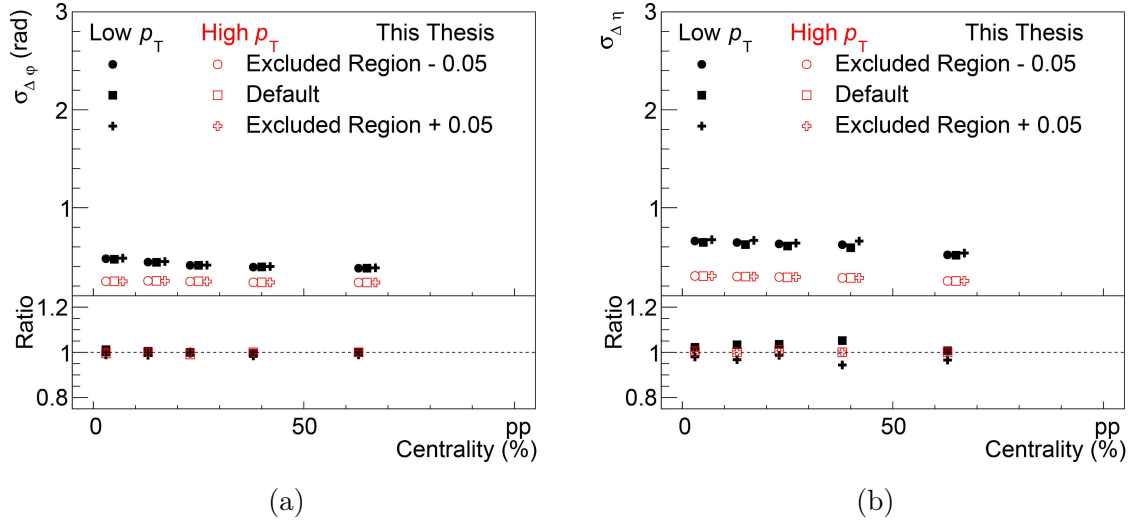


Figure 32: Generalised Gaussian fit results as the function of the size of the excluded region: depletion yield (a) and $\sigma_{\Delta\eta}$ (b) and $\sigma_{\Delta\phi}$ (c) widths at low p_T : $1 \text{ GeV}/c \leq p_{T,trigger}, p_{T,assoc} \leq 2 \text{ GeV}/c$ and at high p_T : $4 \text{ GeV}/c \leq p_{T,trigger} \leq 8 \text{ GeV}/c$ and $2 \text{ GeV}/c \leq p_{T,assoc} \leq 3 \text{ GeV}/c$. (for identified kaon)

5.5 Tracking inefficiencies

As it was presented in Section 5.1 I calculated the correction for the tracking inefficiencies. In this section, I will compare the obtained corrected results with the uncorrected ones. The corrections in the case of the angular correlation analysis taken at $\sqrt{s_{NN}} = 2.76$ TeV centre-of-mass energy per nucleon pair do not affect the obtained results. Figs. 33, 34 shows the difference between the results with and without tracking inefficiencies for the $\sigma_{\Delta\varphi}$, $\sigma_{\Delta\eta}$ and the depletion yield. The figures demonstrates that the deviation between the obtained values are below $\approx 5\%$. To conclude this, the corrections do not influence the results.

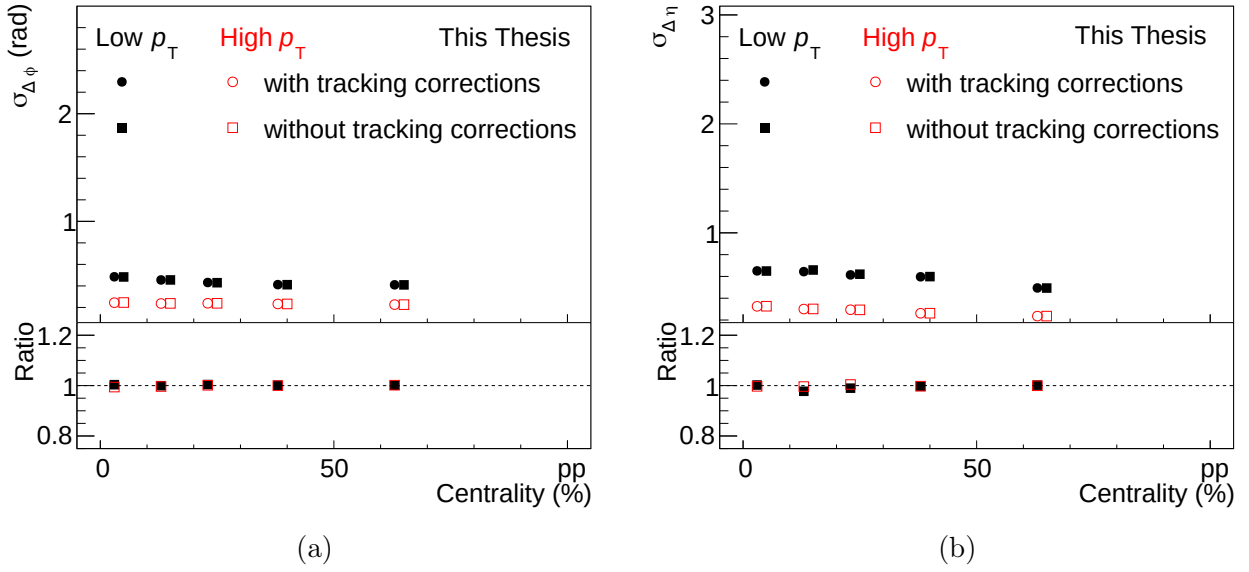


Figure 33: Generalised Gaussian fit results as the function the tracking inefficiencies correction: $\sigma_{\Delta\eta}$ (b) and $\sigma_{\Delta\varphi}$ (a) widths at low p_T : $1 \text{ GeV}/c \leq p_{T,trigger}, p_{T,assoc} \leq 2 \text{ GeV}/c$ and at high p_T : $4 \text{ GeV}/c \leq p_{T,trigger} \leq 8 \text{ GeV}/c$ and $2 \text{ GeV}/c \leq p_{T,assoc} \leq 3 \text{ GeV}/c$. (for unidentified particles)

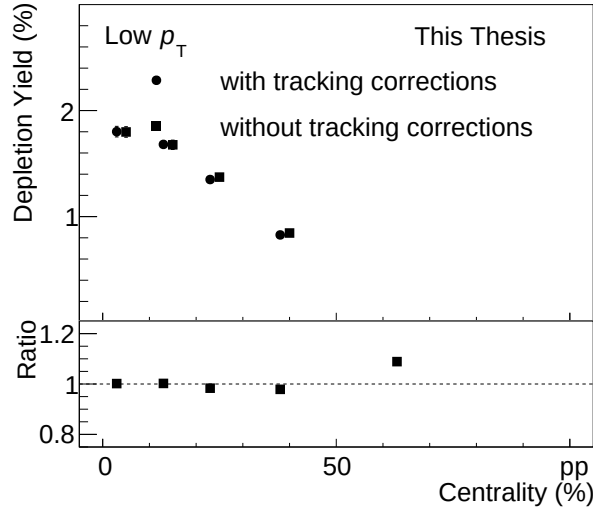


Figure 34: Depletion yield results as the function of z -vertex range at low p_T : $1 \text{ GeV}/c \leq p_{T,trigger}, p_{T,assoc} \leq 2 \text{ GeV}/c$ and at high p_T : $4 \text{ GeV}/c \leq p_{T,trigger} \leq 8 \text{ GeV}/c$ and $2 \text{ GeV}/c \leq p_{T,assoc} \leq 3 \text{ GeV}/c$. (for identified kaon)

6 ALICE data analysis

In this chapter, the results from the method demonstrated in Section 5. are presented. Fig. 35 shows the results of the width of the near-side peak from the generalised Gaussian fit for both the $\Delta\varphi$ and the $\Delta\eta$ directions as a function of centrality and transverse momentum. The figure shows that the near-side jet peak has a significant p_T and centrality dependence. However, the width is independent of the centrality, in the highest p_T bin. Furthermore, the broadening is stronger in the direction of $\Delta\eta$ than in $\Delta\varphi$. I also calculated the near-side peak from kaon K^\pm (Fig. 37) and pion π^\pm (Fig. 36) identified angular correlations. The results from these correlations show similar trends as in the case of the unidentified correlation. The deviation between the identified and unidentified results is larger in the direction of $\Delta\eta$ than in the direction of $\Delta\varphi$. It is important to notice that the widths in the direction of $\Delta\eta$ are smaller for both identified cases than the unidentified one. The explanation presumably comes from the fact that protons have a large contribution to the near-side jet peak and their near-side jet peak width is larger than the unidentified case. This assumption comes from the AMPT simulations and has to be studied further. Furthermore, the Fig. 36 and Fig. 37 demonstrate that the widths of jet peaks are smaller in the case of pions than in the case of kaons.

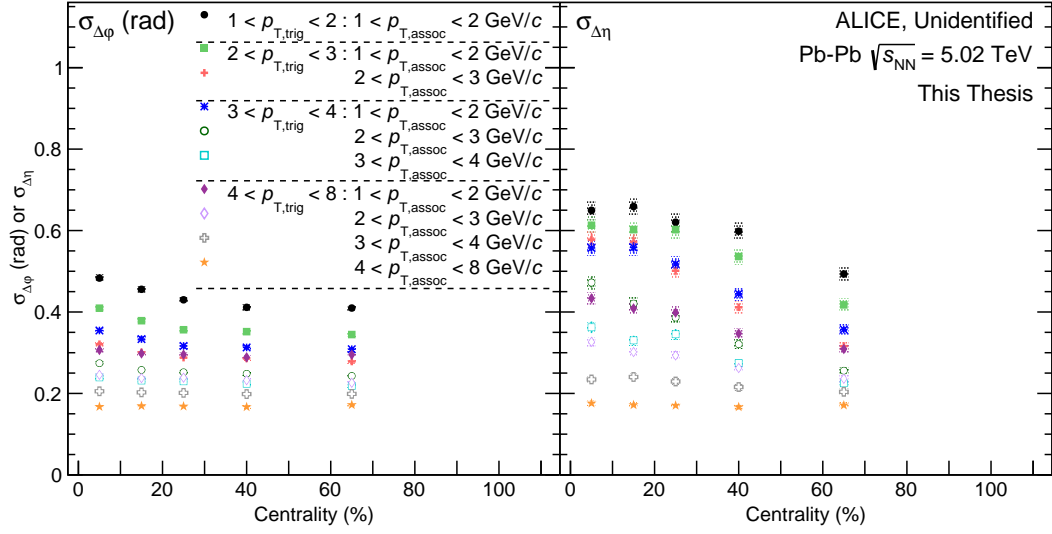


Figure 35: Width of the near-side jet peak in Pb–Pb collisions at $\sqrt{s_{NN}} = 5.02$ TeV from unidentified hadron-hadron angular correlations. The left panel shows the width in the $\Delta\varphi$ direction (right), while the right panel in the $\Delta\eta$ direction (left). Error bars show the statistical uncertainties, while the shaded areas represent the systematical uncertainties.

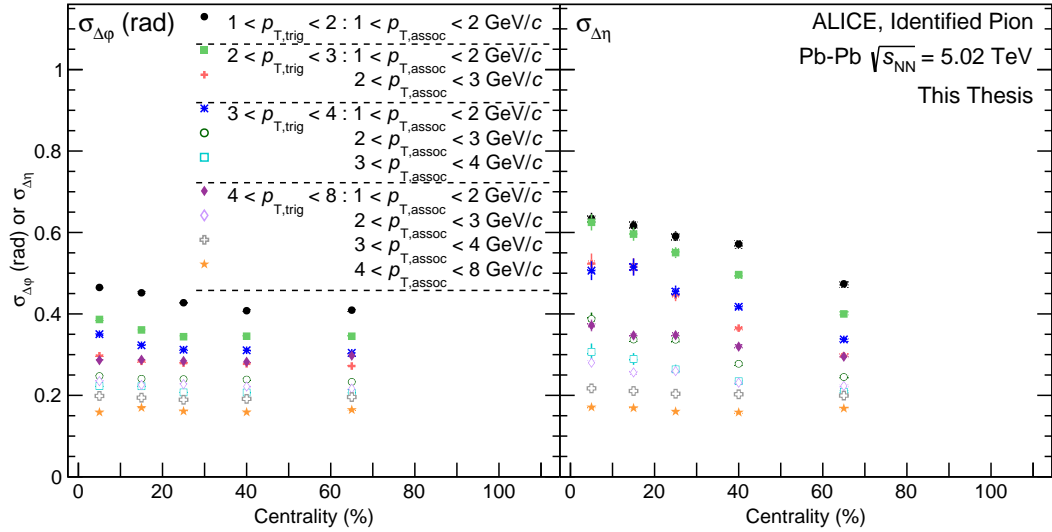


Figure 36: Width of the near-side jet peak in Pb–Pb collisions at $\sqrt{s_{NN}} = 5.02$ TeV from identified pion-hadron angular correlations. The left panel shows the width in the $\Delta\varphi$ direction (right), while the right panel in the $\Delta\eta$ direction (left). Error bars show the statistical uncertainties, while the shaded areas represent the systematical uncertainties.

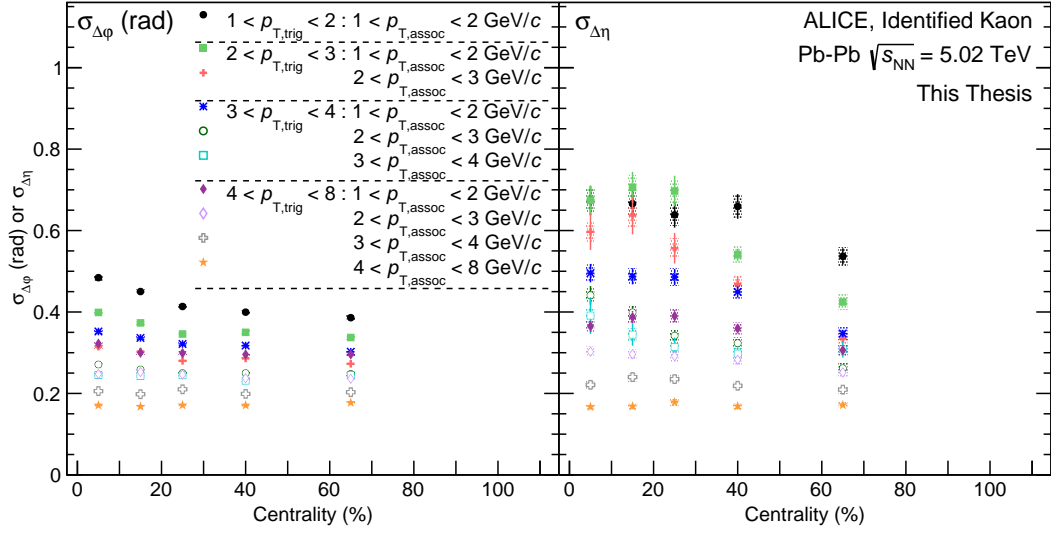


Figure 37: Width of the near-side jet peak in Pb–Pb collisions at $\sqrt{s_{NN}} = 5.02$ TeV from identified kaon-hadron angular correlations. The left panel shows the width in the $\Delta\phi$ direction (right), while the right panel in the $\Delta\eta$ direction (left). Error bars show the statistical uncertainties, while the shaded areas represent the systematical uncertainties.

In order to compare the different broadening trends of the width of the near-side jet peak, I studied how the values in the most central bin (0–10%) are proportional to the values obtained in the most peripheral (50–80%) ones in both directions. I denoted these values by $\sigma_{\Delta\phi}^{CP}$ and $\sigma_{\Delta\eta}^{CP}$. Systematic uncertainties were calculated from the errors of the widths of the near-side jet peak by the propagation of uncertainty. These results from $\sqrt{s_{NN}} = 5.02$ TeV Pb-Pb collision can be seen in Fig. 38. The obtained results show that there are bigger differences in case of the $\Delta\phi$ direction. I also compared these results with the results measured at $\sqrt{s_{NN}} = 2.76$ TeV collision energy by the ALICE Collaboration [37], which can be seen in Fig. 39. The comparison of the σ^{CP} values show that the trends of the unidentified jet peak results are independent of the centre-of-mass energy, but the σ^{CP} values are different for few p_T cases in $\Delta\eta$ direction.

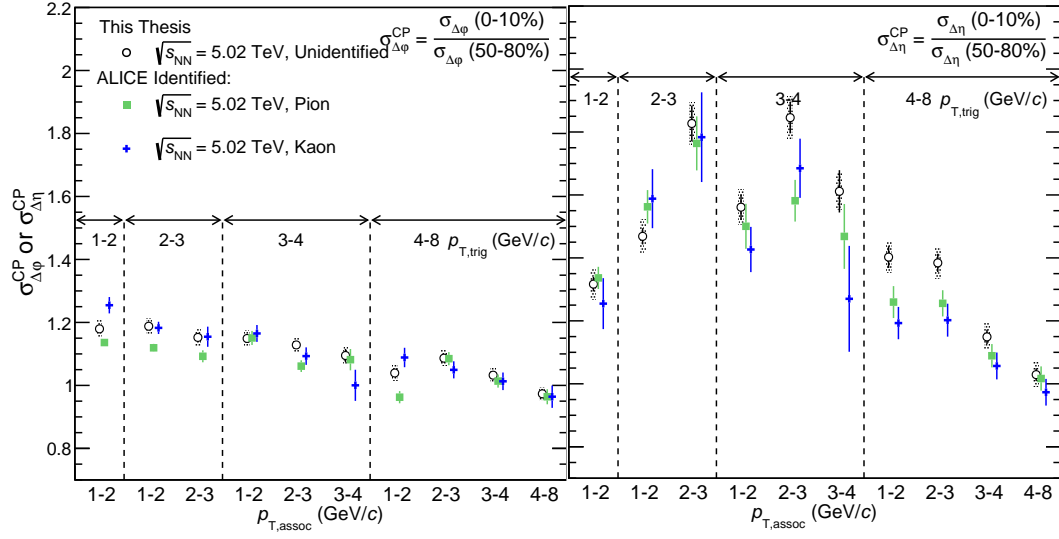


Figure 38: The $\sigma_{\Delta\phi}^{CP}$ (left) $\sigma_{\Delta\eta}^{CP}$ (right) results from Pb-Pb collision at $\sqrt{s_{NN}} = 5.02$ TeV centre-of-mass energy as a function of the transverse momenta p_T and centrality. Error bars (mostly smaller than the marker size) show the statistical uncertainties, while the shaded areas represent the systematical uncertainties.

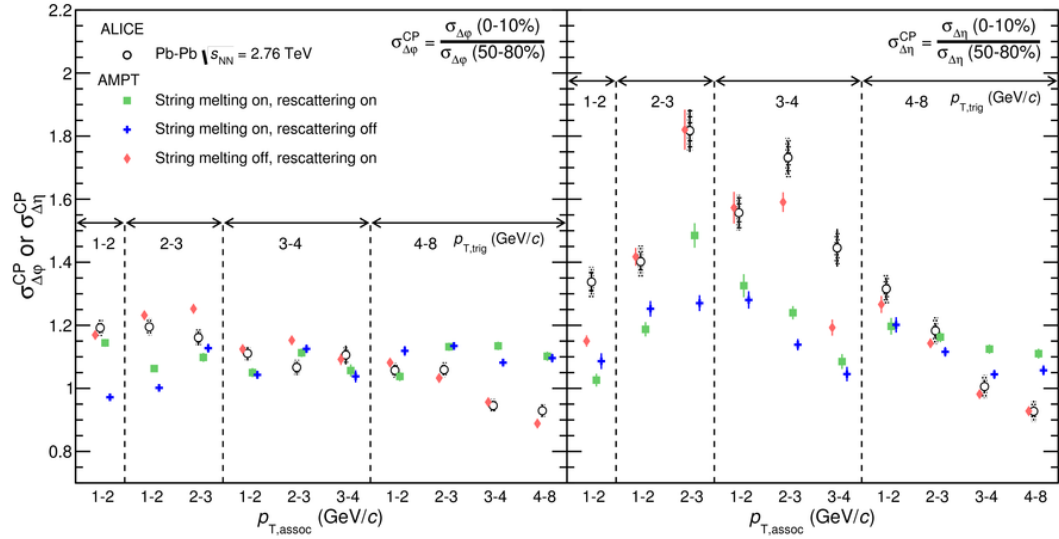


Figure 39: The σ^{CP} results at $\sqrt{s_{NN}} = 2.76$ TeV Pb-Pb collision energy measured by the ALICE Collaboration [37]. Error bars (mostly smaller than the marker size) show the statistical uncertainties, while the shaded areas represent the systematical uncertainties.

In the next step, I studied the depletion yield as the function of the centrality and the particle species. The obtained results can be seen on Fig. 40 and Fig. 41. The figures demonstrate that the depletion yield has a strong particle species dependence. It is almost non-existent (less than 0.3%) for the lightest pions, while there are significant differences between the kaon and the unidentified cases. The figures show that the depletion yield is larger from the unidentified angular correlation. This is presumably due to the fact that the contribution of protons in the unidentified case is much more significant at the low transverse momenta, which can significantly increase the extent of the depletion yield.

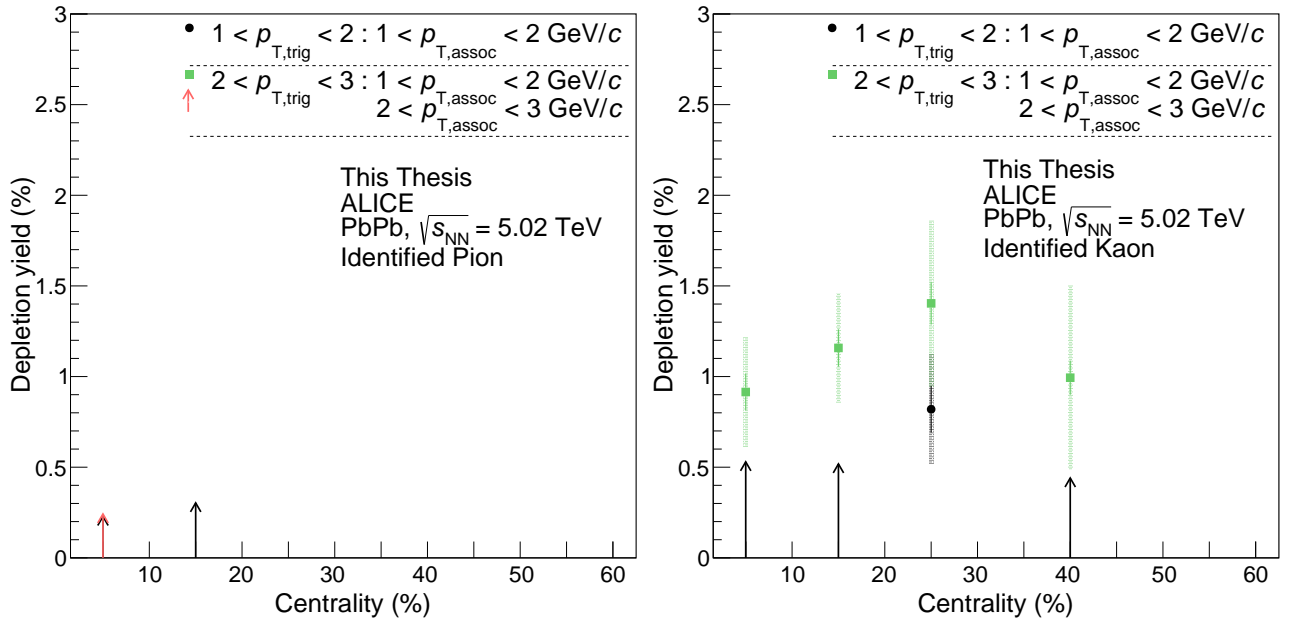


Figure 40: The depletion yield as a function of centrality and p_T from identified pion (left) and identified kaon (right) correlations. The full lines represent the statistical uncertainties and the shaded regions indicate the systematical uncertainties. The arrows represent an upper limit for the depletion yield in the cases where the band of the systematic uncertainty touches zero.

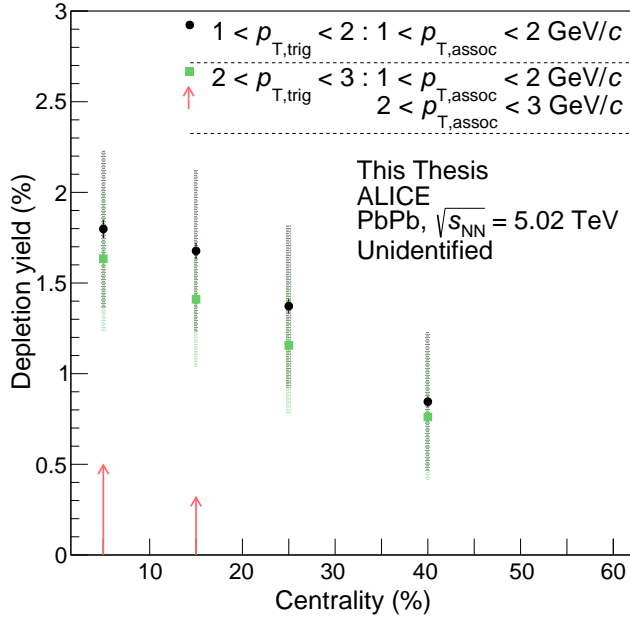


Figure 41: The depletion yield as a function of centrality and p_T from unidentified angular correlations. The full lines represent the statistical uncertainties and the shaded regions indicate the systematical uncertainties. The arrows represent an upper limit for the depletion yield in the cases where the band of the systematic uncertainty touches zero.

7 Results of the AMPT simulations

In this section, I will present my results from the AMPT simulation and compare these results with the ALICE analysis. One can notice, that the identified kaon-hadron two particle angular correlation results are not presented in this section. The reason behind this is that a non-trivial structure appeared in the correlations and the analysis of the origin of this structure is still ongoing. As it was presented in Section 3.1. I used three different setups in AMPT to simulate Pb-Pb collisions at $\sqrt{s_{NN}} = 5.02 \text{ TeV}$ centre-of-mass energy per nucleon pair. The Figs. 42, 43 and 44 show the results from the AMPT simulations with the configurations: string melting off and hadronic rescattering off. The results show that the width of the near-side jet peak in the $\Delta\varphi$ direction is independent from the centrality and from the particle species. In contrary, in the $\Delta\eta$ case, there is a clear jet broadening at the low p_T region. The $\Delta\eta$ figures demonstrate that the jet broadening effect has a clear particle species dependence, the obtained width of the jet peaks are larger in case of the proton-hadron case and smaller in the

pion-hadron case compared to the unidentified one. Unexpectedly, in the most central bins a narrowing was seen compared to the second centrality bin in case of the identified proton-hadron correlation. The origin of these affect is not yet fully understood. Furthermore, the depletion yield did not appear at all in these simulations.

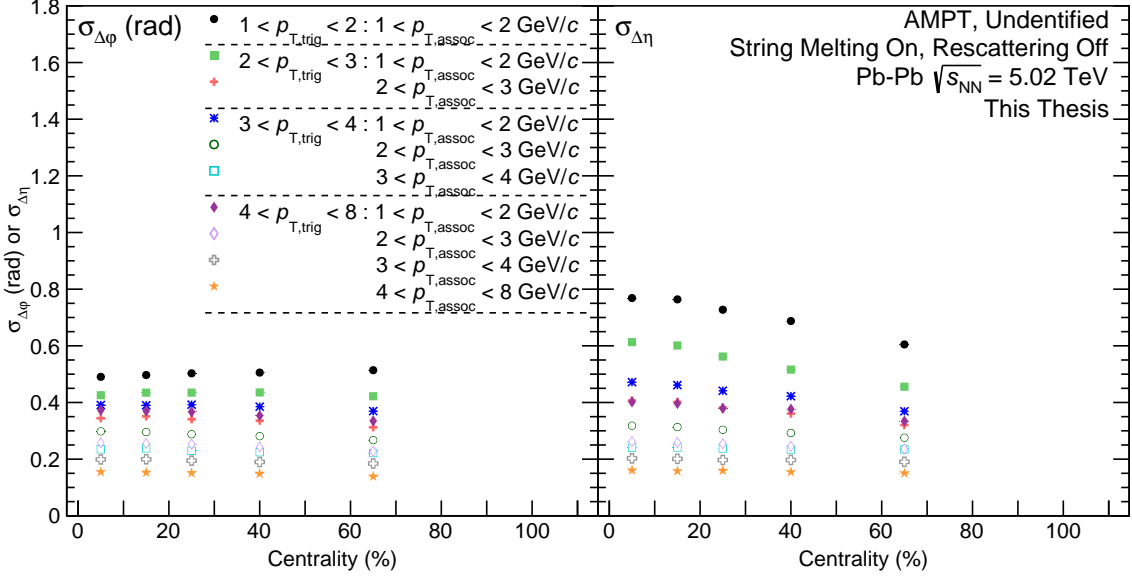


Figure 42: Width of the near-side jet peak in Pb-Pb collisions (AMPT) at $\sqrt{s_{NN}} = 5.02$ TeV from unidentified hadron-hadron angular correlations. The left panel shows the width in the $\Delta\phi$ direction, while the right panel in the $\Delta\eta$ direction.

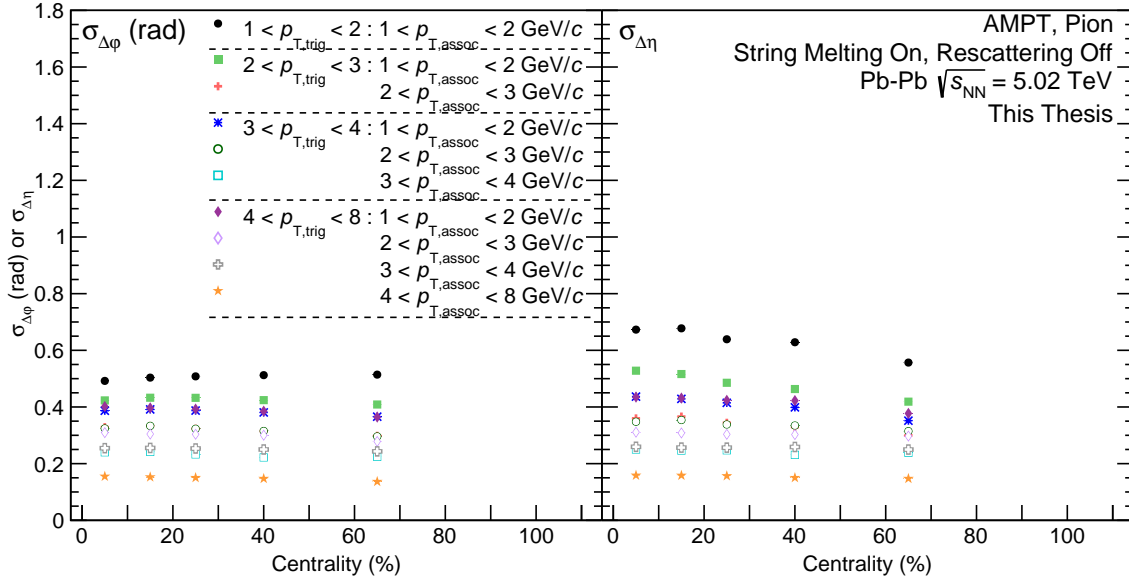


Figure 43: Width of the near-side jet peak in Pb–Pb collisions (AMPT) at $\sqrt{s_{NN}} = 5.02$ TeV from identified pion-hadron angular correlations. The left panel shows the width in the $\Delta\varphi$ direction, while the right panel in the $\Delta\eta$ direction.

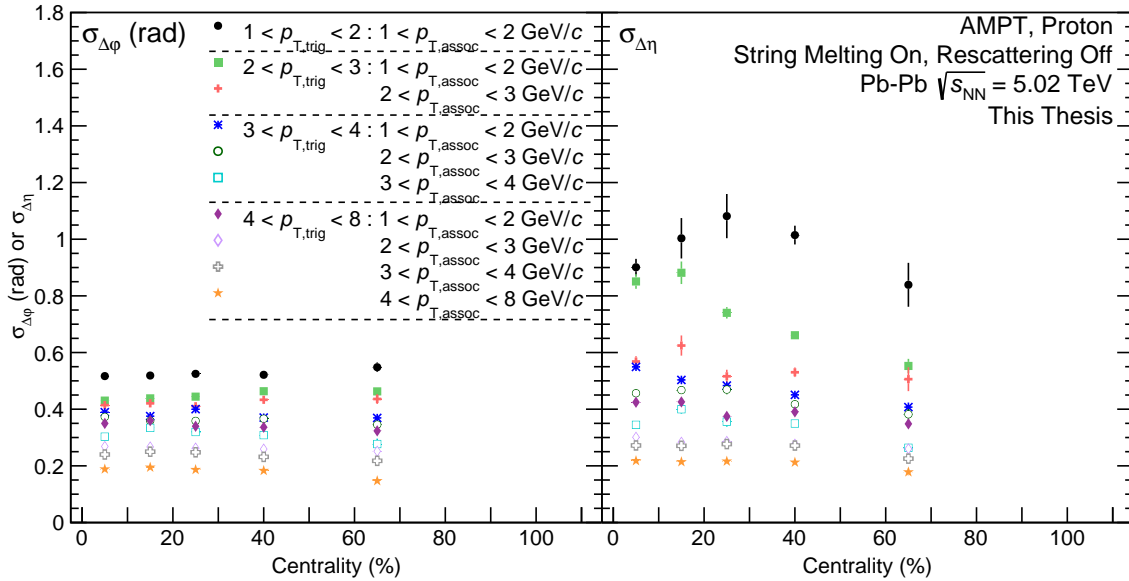


Figure 44: Width of the near-side jet peak in Pb–Pb collisions (AMPT) at $\sqrt{s_{NN}} = 5.02$ TeV from identified proton-hadron angular correlations. The left panel shows the width in the $\Delta\varphi$ direction, while the right panel in the $\Delta\eta$ direction.

In the following step, I would like to quantify the effects of the hadronic rescatterings. Figs. 45, 46 and 47 show the results from the AMPT simulations with the additional ART module, which is responsible for the hadronic rescattering. I did not find an as large jet broadening effect in this configuration as in the previous one. Evidently, the width of the near side jet-peak is independent in $\Delta\varphi$ from the centrality and the particle species. The additional use of the ART model causes smaller centrality dependence of the width in $\Delta\eta$, however the generalised Gaussian fit did not work perfectly for the central bins for the three lowest p_T cases of the identified proton-hadron correlation. The most striking observation is that if we add hadronic interactions to the simulation, the depletion yield appears. Moreover, Fig. 48 shows that the depletion yield has a significant centrality and particle species dependence.

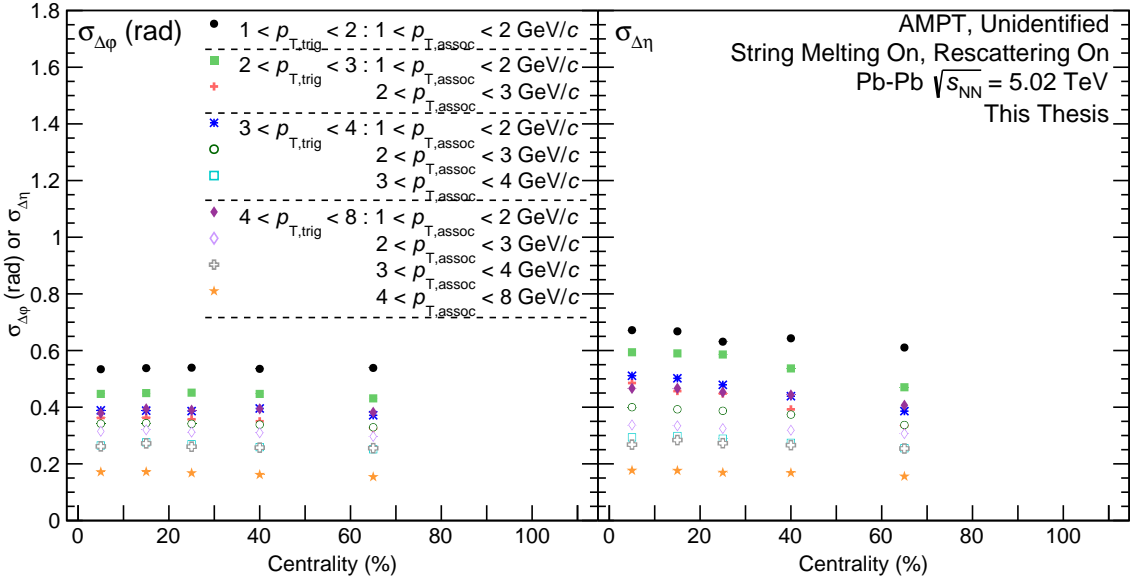


Figure 45: Width of the near-side jet peak in Pb–Pb collisions (AMPT) at $\sqrt{s_{NN}} = 5.02$ TeV from unidentified hadron-hadron angular correlations. The left panel shows the width in the $\Delta\varphi$ direction, while the right panel in the $\Delta\eta$ direction.

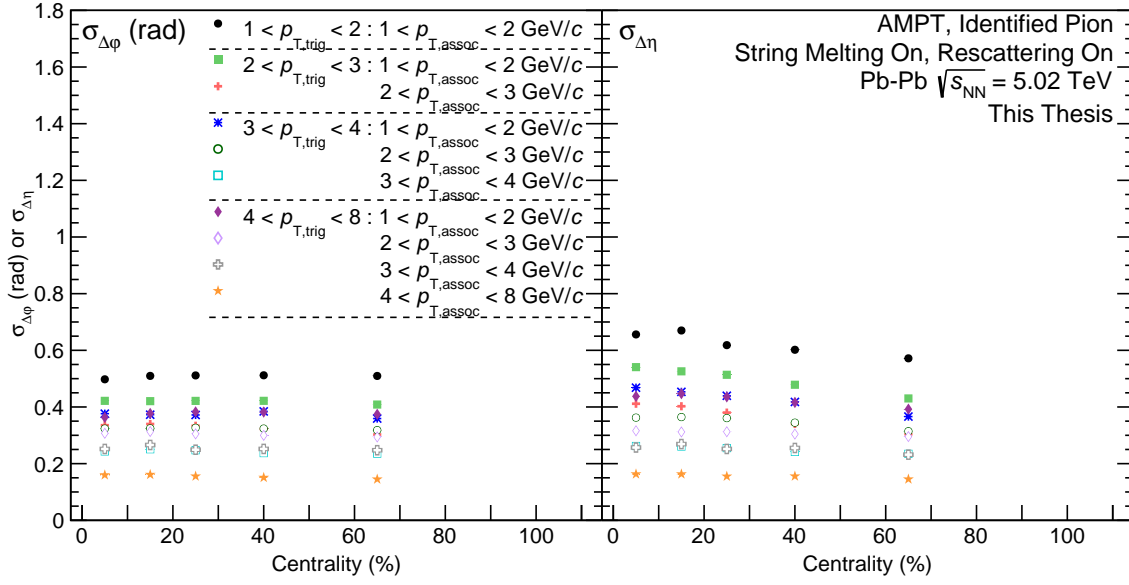


Figure 46: Width of the near-side jet peak in Pb-Pb collisions (AMPT) at $\sqrt{s_{NN}} = 5.02$ TeV from identified pion-hadron angular correlations. The left panel shows the width in the $\Delta\phi$ direction, while the right panel in the $\Delta\eta$ direction.

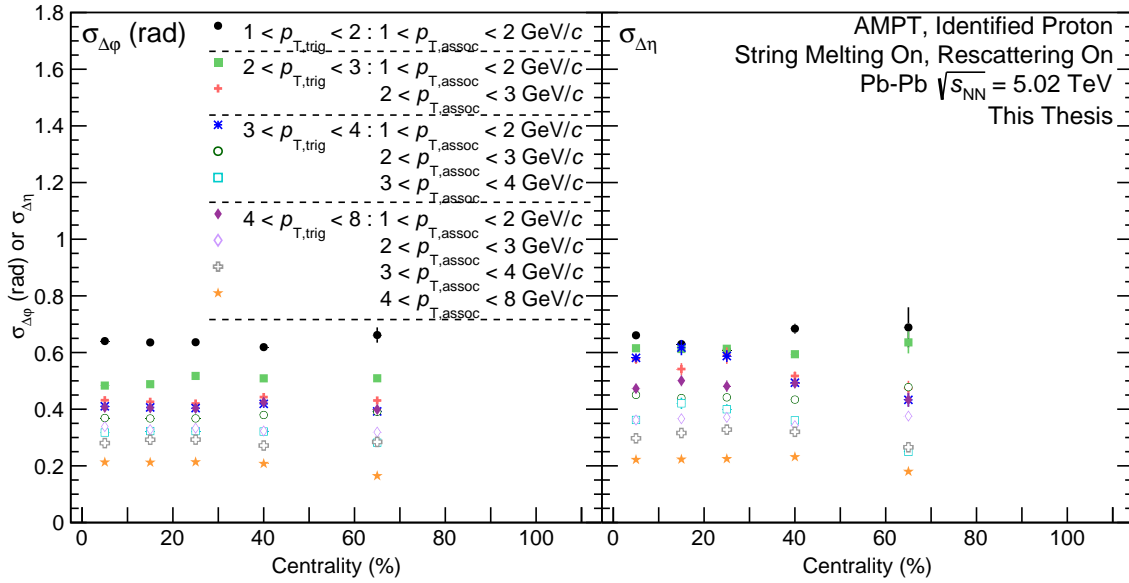
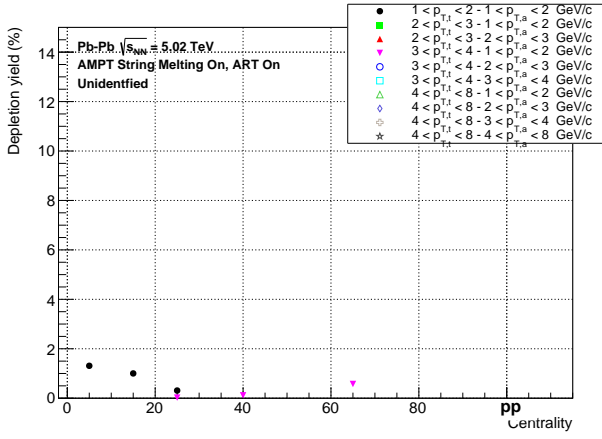
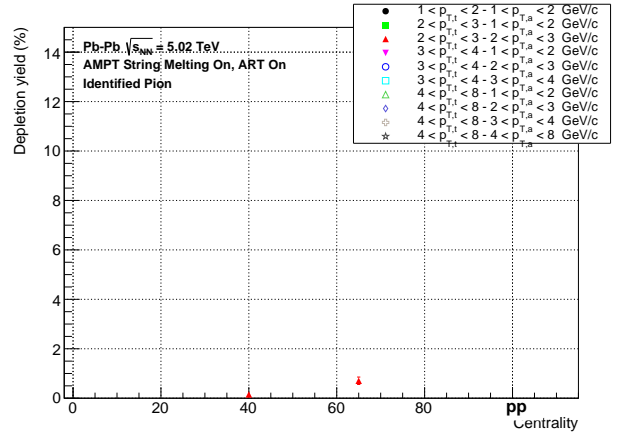


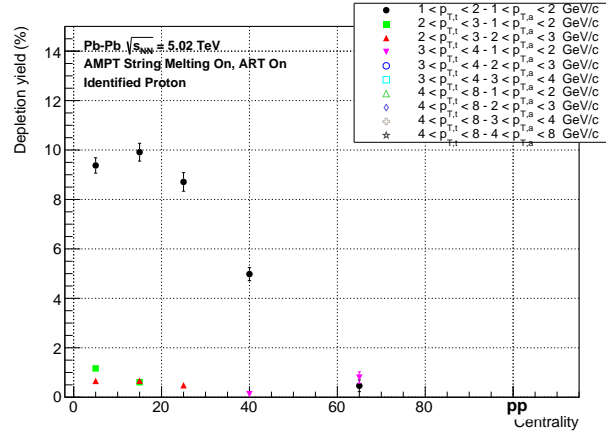
Figure 47: Width of the near-side jet peak in Pb-Pb collisions (AMPT) at $\sqrt{s_{NN}} = 5.02$ TeV from identified proton-hadron angular correlations. The left panel shows the width in the $\Delta\phi$ direction, while the right panel in the $\Delta\eta$ direction.



(a)



(b)



(c)

Figure 48: The depletion yield in Pb-Pb collisions (AMPT) at $\sqrt{s_{NN}} = 5.02$ TeV from a generalised Gaussian fit. Panel (a.) shows the unidentified case, while panel (b.) and (c.) show the identified pion and proton cases respectively.

Finally, I analysed the case where string melting is turned off and the hadronic rescatterings were considered. Figs. 49, 50 and 51 shows the width of the near-side jet-peaks have a significant centrality dependence in both directions. However, the generalised Gaussian fit does not perform well in the 10 – 20% and 20 – 30% centrality bins. I found that the jet broadening effect is stronger in the $\Delta\eta$ direction than in the $\Delta\varphi$ direction. Furthermore, it was found that the proton results are larger and the pion results are smaller than the unidentified values. Fig. 52 shows that the depletion yield has a clear particle species and centrality dependence. It was found that the heaviest proton produces the largest depletion yield. To conclude these simulation results, we can say that the origin of the depletion yield presumably comes from the hadronic interactions. It is important to notice, that in these simulations pions also produce a depletion yield in the angular correlations.

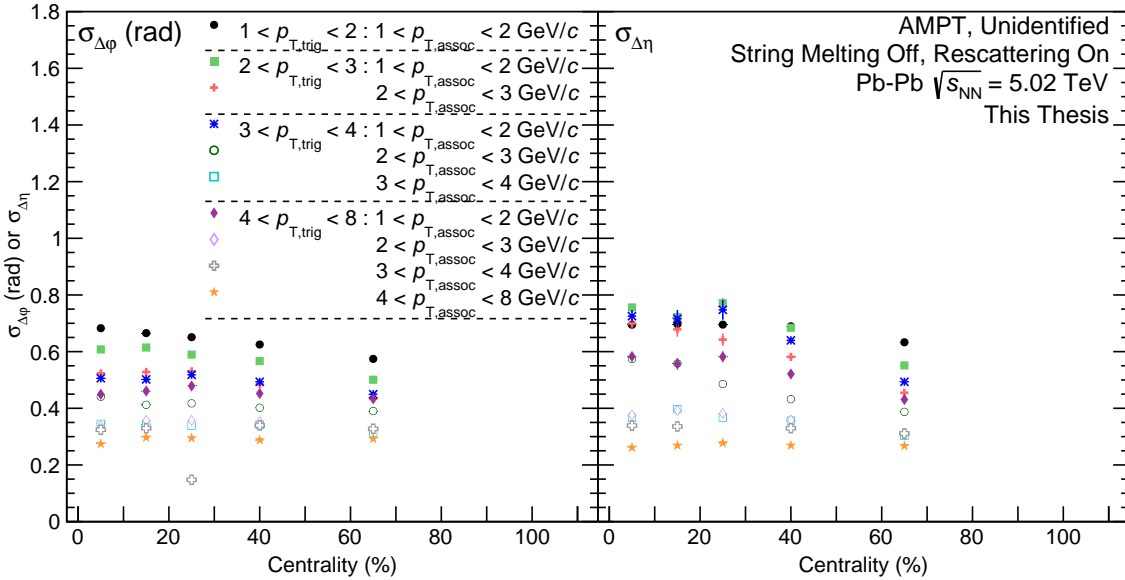


Figure 49: Width of the near-side jet peak in Pb–Pb collisions (AMPT) at $\sqrt{s_{NN}} = 5.02$ TeV from unidentified hadron-hadron angular correlations. The left panel shows the width in the $\Delta\varphi$ direction, while the right panel in the $\Delta\eta$ direction.

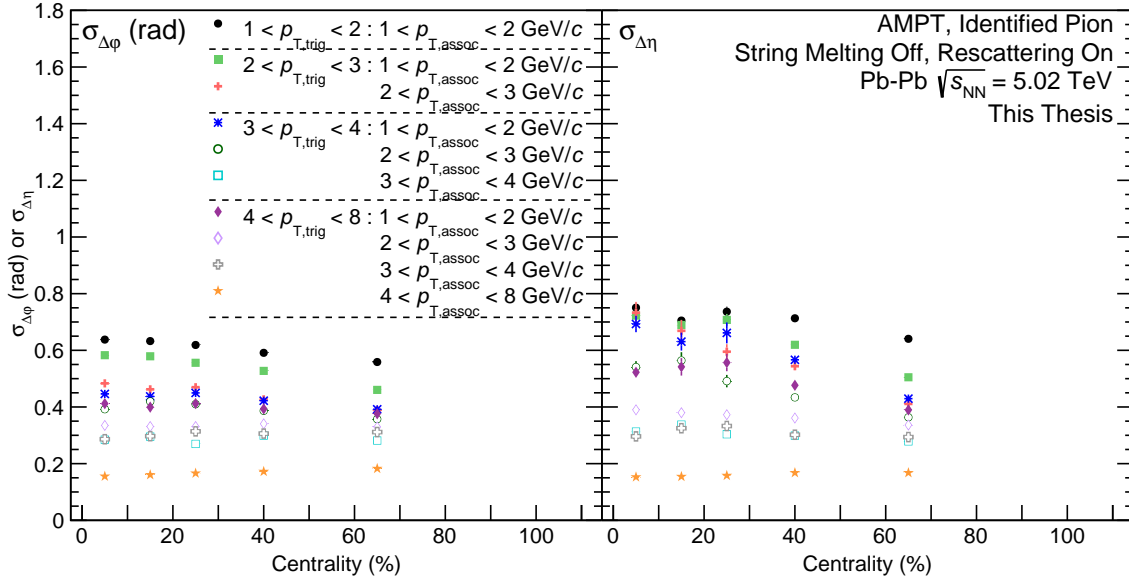


Figure 50: Width of the near-side jet peak in Pb-Pb collisions (AMPT) at $\sqrt{s_{NN}} = 5.02$ TeV from identified pion-hadron angular correlations. The left panel shows the width in the $\Delta\phi$ direction, while the right panel in the $\Delta\eta$ direction.

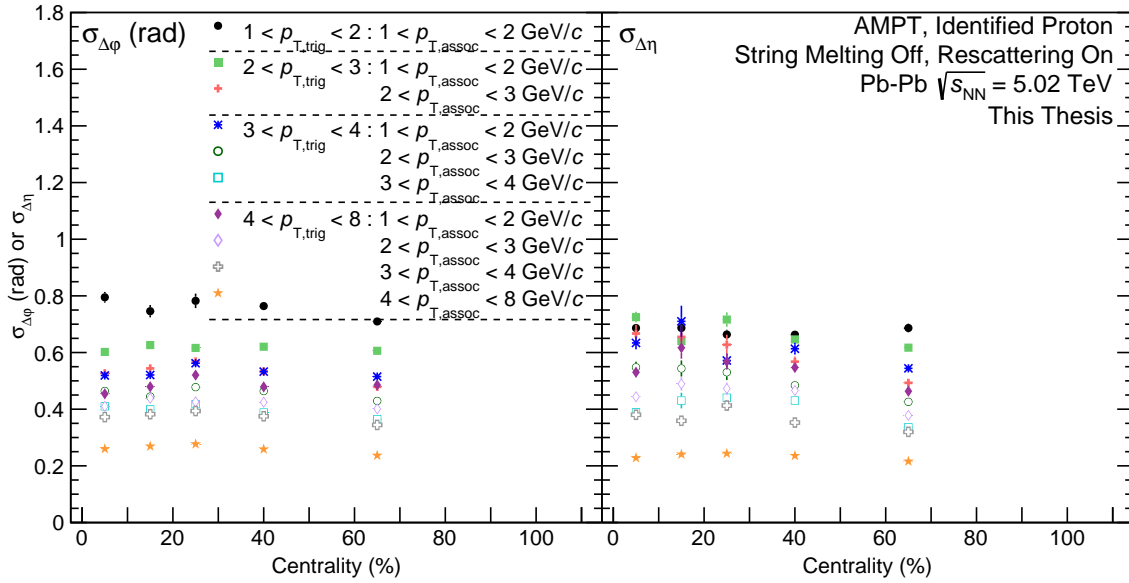
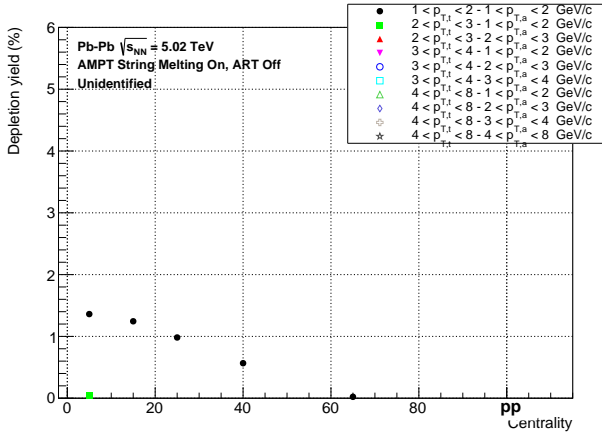
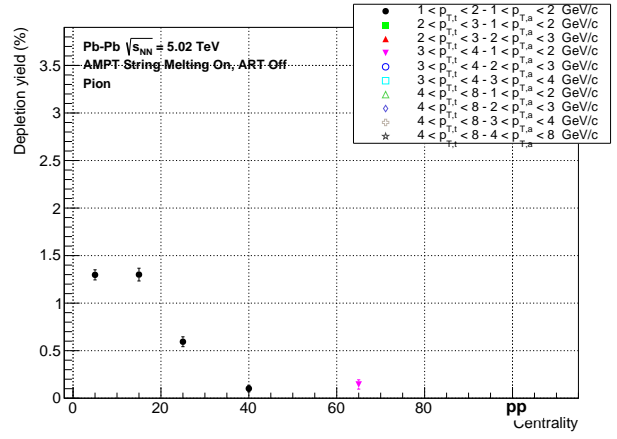


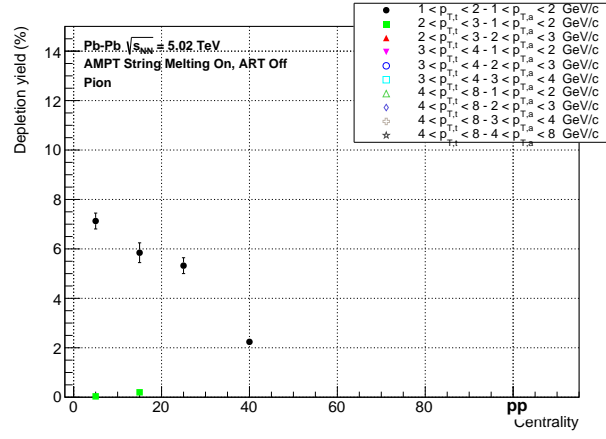
Figure 51: Width of the near-side jet peak in Pb-Pb collisions (AMPT) at $\sqrt{s_{NN}} = 5.02$ TeV from identified proton-hadron angular correlations. The left panel shows the width in the $\Delta\phi$ direction, while the right panel in the $\Delta\eta$ direction.



(a)



(b)



(c)

Figure 52: The depletion yield in Pb-Pb collisions (AMPT) at $\sqrt{s_{NN}} = 5.02$ TeV from a generalised Gaussian fit. Panel (a.) shows the unidentified case, while panel (b.) and (c.) show the identified pion and proton cases respectively.

To understand the physical relevance of these simulation, we shall compare these results with the ALICE measurements. To achieve this goal I used $\sigma_{\Delta\eta}^{CP}$ and $\sigma_{\Delta\varphi}^{CP}$ quantities. Comparison between the unidentified and identified pion-hadron correlation measurements in ALICE and in all three AMPT configurations can be seen in Fig. 53 and Fig. 54 respectively. One can notice, that the configuration where string melting processes are turned off describes the experimental results best. Besides that, the other two simulation configuration describe the measured data quite well. Furthermore, we can conclude that the depletion structure does not appear, if the interactions between hadrons are not considered in the simulations. So we can presume from these simulations that one of the main source of this phenomena is the effect of hadronic scatterings. Although, in the previous simulation pions also creates depletion, which is not the case in the experimental results.

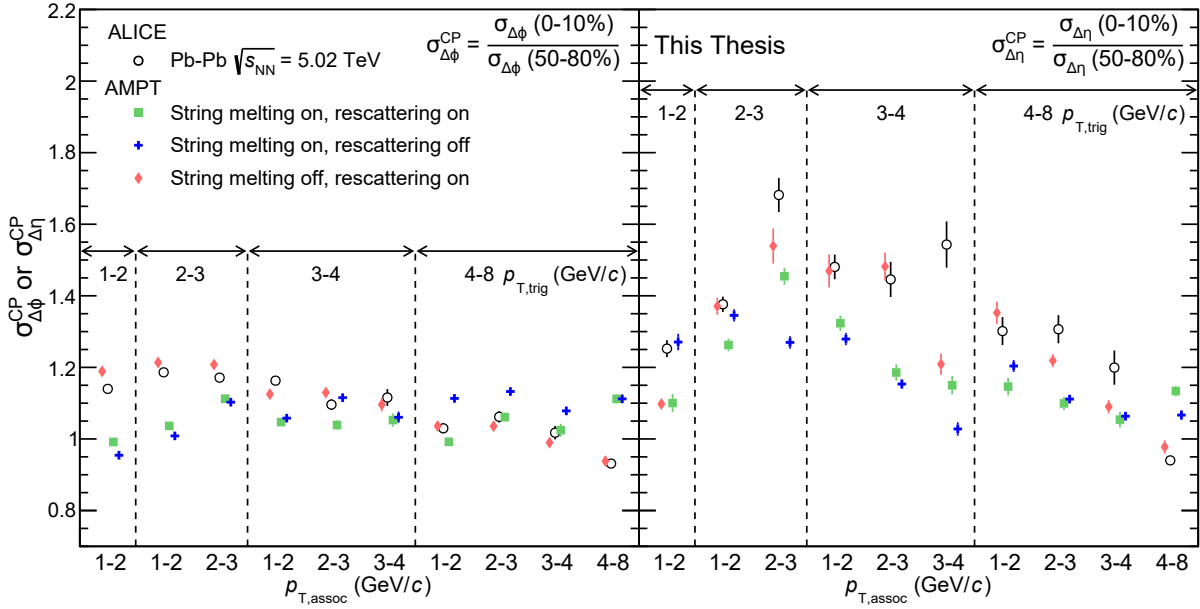


Figure 53: The $\sigma_{\Delta\varphi}^{CP}$ (left) $\sigma_{\Delta\eta}^{CP}$ (right) results from Pb-Pb collision at $\sqrt{s_{NN}} = 5.02$ TeV centre-of mass energy as a function of transverse momenta p_T and centrality for unidentified particles

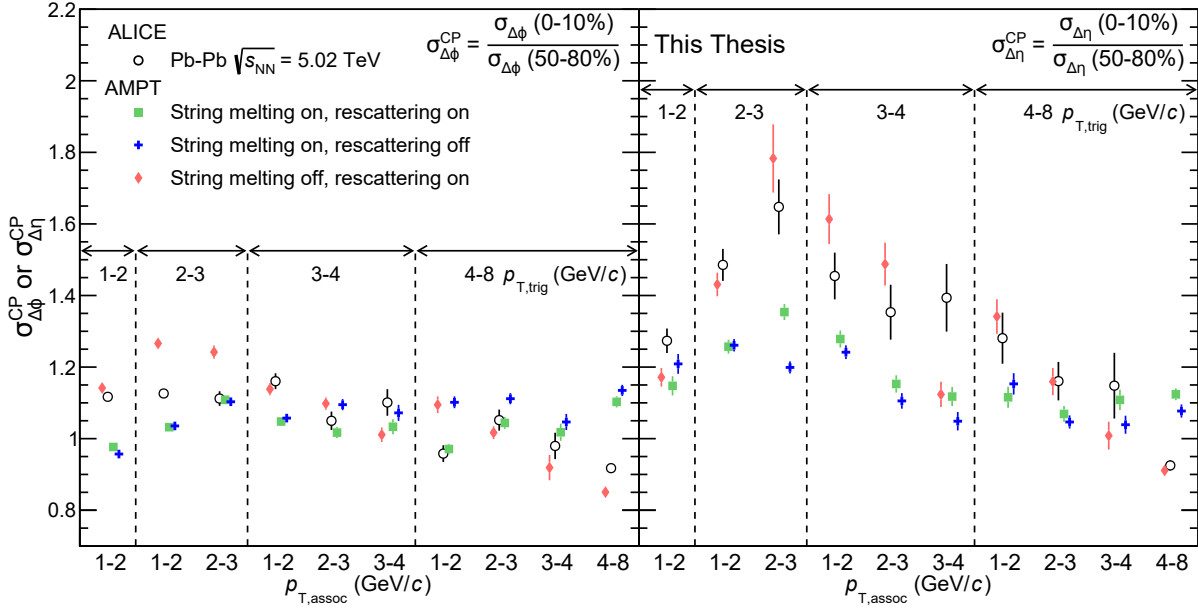


Figure 54: The $\sigma_{\Delta\phi}^{CP}$ (left) $\sigma_{\Delta\eta}^{CP}$ (right) results from Pb-Pb collision at $\sqrt{s_{NN}} = 5.02$ TeV centre-of mass energy as a function of transverse momenta p_T and centrality for identified pions.

8 Summary

In my thesis, I studied identified and unidentified two-particle angular correlations of Pb-Pb collisions at $\sqrt{s_{NN}} = 5.02$ TeV collision energy recorded by the ALICE Collaboration in 2018. I determined the $\sigma_{\Delta\phi}$ and $\sigma_{\Delta\eta}$ widths of the near-side jet peak and the depletion yield by a fit with a generalised Gaussian function. In addition to this, I determined the systematic uncertainties occurring during fitting. Furthermore I studied the dependence of the broadening of the near-side jet peak and the depletion yield in the ALICE experiment at $\sqrt{s_{NN}} = 5.02$ TeV centre-of-mass energy. Moreover I examined these phenomena's dependence on the particle species. Results showed that compared to the unidentified case significant differences occur both in the value of the width and the depletion yield. It is visible that the width values in the identified cases are lower than in the unidentified ones. In order to shed light on the reason of this phenomenon, the contribution from protons need to be determined. The deviation from the generalised Gauss-shape is not present in case of pions, while it is significant for the kaons and the unidentified case. The AMPT simulations show that the depletion yield presumably occurred from the effect of the hadronic scatterings, because depletion only appeared when the hadronic interactions were turned on. We can conclude that the configuration where string

melting processes are turned off and the hadronic rescatterings were considered described the experimental data the best. Although, in this case pions also generate depletion yield, which is not true in the case of the experimental measurements. In the future, the purity tests are still needed to be performed and correction has to be made for the identified proton-hadron angular correlations (in ALICE) and for the identified kaon-hadron angular correlation (in AMPT) to finalise this analysis.

9 Összefoglalás

A dolgozatomban a 2018-ban az ALICE detektor által $\sqrt{s_{NN}} = 5.02$ TeV ütközési energián felvett ólom-ólom adatain végeztem azonosítatlan, illetve azonosított kétrészecske-szögkorrelációs analízist. Egy általánosított gauss-függvény illesztésével meghatároztam a kapott jet-csúchoz tartozó $\sigma_{\Delta\varphi}$, $\sigma_{\Delta\eta}$ szélesség értékeket és a keresett kráter struktúra mértékét. Ezen felül meghatároztam az illesztés során felmerülő szisztematikus hibákat. Dolgozatomban vizsgáltam, hogy az ALICE kísérletben mért jet-kiszéledés és kráter struktúra, hogyan függ a centralitástól és a transzverzális impulzustól $\sqrt{s_{NN}} = 5.02$ TeV ütközési energián, illetve vizsgáltam ezen kérdéses jelenségek részecsketípus függését. A kapott eredmények azt mutatják, hogy az azonosítatlan esethez képest jelentős eltérés tapasztalható, mind a szélesség értékekben, mind a kráter struktúra méretében. Megfigyelhető, hogy az azonosított esetben az azonosított képest kapott értékeket. Annak érdekében, hogy ezen jelenség okára rávilágíthassunk szükséges lesz a protonokból származó járulékok meghatározására. A pionok esetében nem tapasztalható az általánosított Gauss-alaktól való eltérés, míg kaonok esetében ennek mértéke jelentős. A kaonok és az azonosítatlan esett között tapasztalt eltérés meghatározásához szintén szükségünk van a protonokból származó járulékok meghatározásához, ennek analízise jelenleg már zajlik. Az AMPT eredményekből következtethetünk arra, hogy a tapasztalt kráter struktúra erősen függ a hadronikus szóródásoktól. Összefoglalva a szimulációs eredményeket azt láthatjuk, hogy az utolsó szimulációs beállítás (string melting off, hadronic rescattering on) írja le legjobban a kapott kísérleti eredményeket. Azonban ezen szimulációk a kráter struktúra megjelenik az azonosított pion szögkorrelációk esetében is, ami ellentétes a kísérleti adatokkal. A továbbiakban az analízis véglegesítéséhez szükséges még a tisztaság tesztek elvégzése, illetve a korrekciók meghatározására az azonosított proton szögkorrelációkban (ALICE) és az azonosított kaon-hadron szögkorrelációkban (AMPT).

Acknowledgements

This research was made possible by the Wigner GPU laboratory, and it was benefited from the grant: NKFIH/OTKA K 120660 and ÚNKP-19-2-I-ELTE-827. I would like to thank the following people for their support, without whose help this work would never have been possible: Gergely Gábor Barnaföldi, Róbert Vértesi and Gábor Bíró. I am particularly grateful to my supervisor Mónika Varga-Kőfaragó for her help, support and for mentoring me over the years. I also wish to thank Márton Nagy, who give me much valuable advice.

References

- [1] J. D. Bjorken. Asymptotic sum rules at infinite momentum. *Physical Review*, 179:1547–1553, 1969.
- [2] David J. Gross and Frank Wilczek. Ultraviolet Behavior of Nonabelian Gauge Theories. *Phys. Rev. Lett.*, 30:1343–1346, 1973.
- [3] T. Ludlam and S. Aronson. Hunting the quark gluon plasma. 4 2005.
- [4] Relativistic heavy-ion collider at the brookhaven national laboratory. Available at <https://www.bnl.gov/rhic>.
- [5] Edward V. Shuryak. Quantum Chromodynamics and the Theory of Superdense Matter. *Phys. Rept.*, 61:71–158, 1980.
- [6] Yasuyuki Akiba et al. The Hot QCD White Paper: Exploring the Phases of QCD at RHIC and the LHC. 2 2015.
- [7] Betty Abelev et al. Centrality determination of Pb-Pb collisions at $\sqrt{s_{NN}} = 2.76$ TeV with ALICE. *Phys. Rev. C*, 88(4):044909, 2013.
- [8] K. Rabbertz. *Jet Physics at the LHC: The Strong Force beyond the TeV Scale*. Springer Tracts in Modern Physics. Springer International Publishing, 2016.
- [9] Michael E. Peskin and Daniel V. Schroeder. *An Introduction to quantum field theory*. Addison-Wesley, Reading, USA, 1995.

- [10] John Harris. Introduction to hard scattering processes and recent results from hard probes at rhic and lhc. *Journal of Physics: Conference Series*, 630, 07 2015.
- [11] David d’Enterria. Jet quenching in QCD matter: From RHIC to LHC. *Nucl. Phys. A*, 827:356C–364C, 2009.
- [12] A. Majumder and M. Van Leeuwen. The Theory and Phenomenology of Perturbative QCD Based Jet Quenching. *Prog. Part. Nucl. Phys.*, 66:41–92, 2011.
- [13] M. Gyulassy, P. Levai, and I. Vitev. NonAbelian energy loss at finite opacity. *Phys. Rev. Lett.*, 85:5535–5538, 2000.
- [14] The ALICE Collaboration. Suppression of charged particle production at large transverse momentum in central pb-pb collisions at $\sqrt{s_{\text{NN}}} = 2.76 = 2.76$ tev. *Phys. Lett. B*, 696:30–39, 12 2010.
- [15] Jaroslav Adam et al. Pseudorapidity dependence of the anisotropic flow of charged particles in Pb-Pb collisions at $\sqrt{s_{\text{NN}}} = 2.76$ TeV. *Phys. Lett. B*, 762:376–388, 2016.
- [16] Jaroslav Adam et al. Azimuthal anisotropy of charged jet production in $\sqrt{s_{\text{NN}}} = 2.76$ TeV Pb-Pb collisions. *Phys. Lett. B*, 753:511–525, 2016.
- [17] Andy Buckley et al. General-purpose event generators for LHC physics. *Phys. Rept.*, 504:145–233, 2011.
- [18] M. Dittmar et al. Introduction to Parton Distribution Functions. In *HERA and the LHC: A Workshop on the Implications of HERA for LHC Physics: CERN - DESY Workshop 2004/2005 (Midterm Meeting, CERN, 11-13 October 2004; Final Meeting, DESY, 17-21 January 2005)*, pages 43–45, Geneva, 2005. CERN.
- [19] Ramona Vogt. *Ultrarelativistic heavy-ion collisions*. Elsevier, Amsterdam, 2007.
- [20] Michael L. Miller, Klaus Reygers, Stephen J. Sanders, and Peter Steinberg. Glauber modeling in high energy nuclear collisions. *Ann. Rev. Nucl. Part. Sci.*, 57:205–243, 2007.
- [21] Bo Andersson, G. Gustafson, G. Ingelman, and T. Sjostrand. Parton Fragmentation and String Dynamics. *Phys. Rept.*, 97:31–145, 1983.

- [22] Monika Varga-Kofarago. *Anomalous Broadening of jet peak Shapes in Pb–Pb Collisions and Characterization of Monolithic Active Pixel Sensors for the ALICE Inner Tracking System Upgrade*. PhD thesis, 2018.
- [23] Torbjörn Sjöstrand. *The Development of MPI Modeling in Pythia*, pages 191–225. 12 2018.
- [24] Zi-Wei Lin, Che Ming Ko, Bao-An Li, Bin Zhang, and Subrata Pal. A Multi-phase transport model for relativistic heavy ion collisions. *Phys. Rev. C*, 72:064901, 2005.
- [25] Large hadron collider and the alice experiment. Available at <http://alice.web.cern.ch/>.
- [26] S. Chatrchyan et al. The CMS Experiment at the CERN LHC. *JINST*, 3:S08004, 2008.
- [27] G. Aad et al. The ATLAS Experiment at the CERN Large Hadron Collider. *JINST*, 3:S08003, 2008.
- [28] Jr. Alves, A. Augusto et al. The LHCb Detector at the LHC. *JINST*, 3:S08005, 2008.
- [29] Betty Bezverkhny Abelev et al. Performance of the ALICE Experiment at the CERN LHC. *Int. J. Mod. Phys. A*, 29:1430044, 2014.
- [30] K. Aamodt et al. The ALICE experiment at the CERN LHC. *JINST*, 3:S08002, 2008.
- [31] Inner tracking system at cern alice experiment. Available at <http://alicematters.web.cern.ch/?q=spdcooling>.
- [32] J. Alme et al. The ALICE TPC, a large 3-dimensional tracking device with fast readout for ultra-high multiplicity events. *Nucl. Instrum. Meth. A*, 622:316–367, 2010.
- [33] Matteo Cacciari, Gavin P. Salam, and Gregory Soyez. The anti- k_t jet clustering algorithm. *JHEP*, 04:063, 2008.
- [34] David d’Enterria. *Jet quenching*, volume 23, page 471. 2010.
- [35] Betty Abelev et al. Measurement of Event Background Fluctuations for Charged Particle Jet Reconstruction in Pb-Pb collisions at $\sqrt{s_{NN}} = 2.76$ TeV. *JHEP*, 03:053, 2012.
- [36] Jaroslav Adam et al. Evolution of the longitudinal and azimuthal structure of the near-side jet peak in Pb-Pb collisions at $\sqrt{s_{NN}} = 2.76$ TeV. *Phys. Rev. C*, 96(3):034904, 2017.

- [37] Jaroslav Adam et al. Anomalous evolution of the near-side jet peak shape in Pb-Pb collisions at $\sqrt{s_{NN}} = 2.76$ TeV. *Phys. Rev. Lett.*, 119(10):102301, 2017.
- [38] Betty Bezverkhny Abelev et al. Performance of the ALICE Experiment at the CERN LHC. *Int. J. Mod. Phys. A*, 29:1430044, 2014.
- [39] Betty Abelev, J. Adam, Dagmar Adamova, M. Aggarwal, Gianluca Aglieri Rinella, A. Agocs, A. Agostinelli, S. Salazar, Zubayer Ahammed, Nora Ahmad, A. Masoodi, S. Ahn, A. Akindinov, D. Aleksandrov, Borri Alessandro, R. Molina, Alici Andrea, Anton Alkin, and M. Zynovyev. Measurement of event background fluctuations for charged particle jet-reconstruction in pb-pb collisions at $\sqrt{s_{NN}} = 2.76$ tev. *Journal of High Energy Physics*, 03:053:1–25, 08 2012.
- [40] Jaroslav Adam et al. Particle identification in ALICE: a Bayesian approach. *Eur. Phys. J. Plus*, 131(5):168, 2016.